https://doi.org/10.5194/egusphere-2026-2295
Preprint. Discussion started: 26 May 2026

On the origin of the twilight color index maximum and its application to cloud-height retrieval

Daniel Toledo [1]

[1]Instituto Nacional de Técnica Aeroespacial INTA, 28850 Torrejon de Ardoz, Spain

Correspondence: Daniel Toledo (toledocd@inta.es)

Abstract. A number of previous studies have demonstrated the capability of detecting high-altitude clouds during twilight using the color index (CI), defined as the ratio of zenith intensities at two different wavelengths, typically selected in the visible range or near infrared (NIR). When high clouds are present, a maximum or minimum (depending on the wavelengths selection) is observed in the CI signal (Sarkissian et al., 1991; Toledo et al., 2016). These studies also showed that the solar zenith angle (SZA) at which the CI maximum or minimum occurs ($\mathrm{SZA}_{\max}$) strongly depends on cloud altitude, enabling cloud-height retrieval through comparison with radiative transfer (RT) simulations. Twilight conditions require RT simulations in spherical geometry, which are computationally expensive. In this work, we introduce a single-scattering formulation of the CI that provides a physically transparent framework for identifying the mechanisms that determine the SZA of the CI maximum and, consequently, the inferred cloud altitude. The simplified formulation is explicitly compared with Monte Carlo RT simulations in spherical geometry and is shown to accurately reproduce the behavior of $\mathrm{SZA}_{\max}$ over a wide range of conditions relevant for high-altitude clouds. In particular, the model provides reliable cloud-height estimates for cloud optical depths up to $\tau_C \lesssim 0.3$. Within this single-scattering formulation, we demonstrate that $\mathrm{SZA}_{\max}$ occurs at the SZA for which the relative SZA-variations of the zenith intensity at the two selected wavelengths become equal, thereby explaining the emergence of the extremum in differential terms. However, achieving a well-defined CI extremum requires selecting two wavelengths with sufficient spectral separation, typically spanning distinct regions of the visible–NIR spectrum. To overcome this spectral dependence, we introduce a Rayleigh-referenced color index (CI^R), defined as the ratio between the measured zenith intensity and the corresponding intensity expected for a purely Rayleigh-scattering atmosphere at the same wavelength. This index reproduces the characteristic extrema associated with high-altitude clouds while requiring simulations and observations at only a single wavelength. The proposed formulation facilitates extensive sensitivity studies and provides greater flexibility in spectral selection, particularly in regions affected by gas absorption.

1 Introduction

Clouds play a major role in Earth climate system through their influence on the planetary radiation budget (Ramanathan et al., 1989). High-altitude clouds such as cirrus clouds, which cover a large fraction of Earth's surface ($\sim 30\,\%$), are especially important because they interact with both incoming solar and outgoing terrestrial radiation (Hartmann et al., 2001). In the visible range, cirrus clouds scatter part of the incident solar radiation back to space (the albedo effect), while in the infrared they

https://doi.org/10.5194/egusphere-2026-2295
Preprint. Discussion started: 26 May 2026

absorb and re-emit terrestrial radiation, contributing to the greenhouse effect. As a result, their overall climatic impact depends strongly on their optical and microphysical properties. Monitoring cirrus clouds through remote sensing observations is therefore essential for characterizing their spatial and temporal variability and for improving their representation in climate models. In addition, since cirrus clouds typically form in the upper troposphere close to the tropopause, determining their altitude can also provide a useful lower bound for the tropopause height.

In addition to cirrus clouds in the upper troposphere, other types of high-altitude clouds also play an important role in atmospheric processes. For instance, polar stratospheric clouds (PSCs), which form in the stratosphere during the cold polar winter, are particularly important because they participate in chemical reactions that lead to ozone depletion. PSCs are composed of supercooled ternary solutions (STS), nitric acid trihydrate (NAT), and/or ice particles (Spang et al., 2018), which provide surfaces for heterogeneous reactions that release reactive chlorine and bromine species that subsequently participate in catalytic ozone destruction cycles. Monitoring PSCs using remote sensing techniques is therefore essential for understanding their composition, microphysics, and variability, as well as for assessing their impact on stratospheric chemistry and ozone layer evolution.

Among the different techniques available for the observation of high-altitude clouds, lidar instruments provide some of the most detailed measurements. Both ground-based and spaceborne lidars, such as the Cloud-Aerosol Lidar with Orthogonal Polarization (CALIOP) (Winker et al., 2009) on board the Cloud-Aerosol Lidar and Infrared Pathfinder Satellite Observations (CALIPSO) satellite, allow the detection of clouds and the retrieval of their vertical structure with high vertical resolution. However, the number of ground-based lidar stations is relatively limited and their geographical coverage remains sparse. For this reason, complementary observational techniques have been developed to investigate high-altitude clouds. Although these techniques generally provide less detailed information about cloud microphysical properties, they can offer valuable insights into their occurrence and variability. In this context, Sarkissian et al. (1991) proposed the use of ground-based UV-VIS spectroscopic observations to detect PSCs and estimate their altitudes during twilight through the analysis of the color index (CI), defined as the ratio between intensities measured at two different wavelengths. This approach was later extended to the detection of cirrus and subvisual cirrus clouds using ground-based optical measurements based on the CI derived from dual-channel radiometric observations (Toledo et al., 2016).

The objective of this work is to investigate the physical basis that explains why the CI can be effectively used for the detection and characterization of high-altitude clouds during twilight. To this end, a new formulation based on the single-scattering approximation is introduced. In addition, methodological improvements are investigated in order to enhance the robustness and applicability of this technique. This study is motivated by recent works in which the CI approach has also been applied to ground-based zenith DOAS observations (Gomez-Martin et al., 2021; Lauster et al., 2022), further demonstrating the potential of twilight measurements for the study of high-altitude aerosol layers. The paper is organized as follows. Section 2 introduces the CI technique and describes how it can be used during twilight for the detection of high-altitude clouds and the estimation of their altitudes. Section 3 presents the new methodology developed in this work to investigate the influence of clouds on the CI signal, as well as an alternative index based on measurements at a single wavelength. Section 4 presents a series of sensitivity analyses, and Section 5 summarizes the main conclusions of this study.

https://doi.org/10.5194/egusphere-2026-2295
Preprint. Discussion started: 26 May 2026

2 The color index approach

The detection and characterization of clouds can be achieved by monitoring the evolution of the CI during twilight. In this work, twilight is defined as the time period when the solar zenith angle (SZA) ranges between 90° and 100°. For a given SZA, the CI is defined as:

$$\mathrm{CI}(\mathrm{SZA}) = \frac{I(\lambda_2, \mathrm{SZA})}{I(\lambda_1, \mathrm{SZA})}, \tag{1}$$

where I represents the intensity at zenith at the wavelengths λ_1 and λ_2, generally selected in the visible or near-infrared range. The presence of high-altitude clouds induces a maximum or a minimum in the CI signal, depending on the choice of λ_1 and λ_2. The SZA at which this maximum or minimum occurs ($\mathrm{SZA_{max}}$) depends on the cloud altitude. To simplify notation, subsequent references to the maximum or minimum in the CI signal will be denoted as $\mathrm{CI_{max}}$. On Earth, $\mathrm{CI_{max}}$ primarily arises from the wavelength dependence of molecular opacity (Rayleigh scattering), as demonstrated in Section 3.1. In the absence of a significant spectral variation of the background atmospheric opacity between the two wavelengths, no pronounced maximum or minimum would be expected in the CI signal. Figure 1 shows examples of CI signals simulated for the Earth atmosphere for different cloud altitudes and different values of λ_1 and λ_2. The simulations were performed using a Monte Carlo RT code, previously employed to model clouds at twilight on Earth (Toledo et al., 2016; Gomez-Martin et al., 2021), Mars (Toledo et al., 2023, 2024), and Titan (West et al., 2016). The simulated CI signals indicate that $\mathrm{SZA_{max}}$ depends on both the cloud altitude (h_C) and the selected wavelengths: the larger λ_2 and h_C, the larger the SZA at which $\mathrm{CI} = \mathrm{CI_{max}}$. Thus, if an instrument measures the intensity at zenith at λ_1 and λ_2, the h_C–$\mathrm{SZA_{max}}$ relation can be computed using a Monte Carlo RT model and subsequently used to derive cloud altitudes from observations of $\mathrm{SZA_{max}}$.

Although this approach for cloud-altitude characterization is straightforward, it relies on three-dimensional RT simulations in spherical geometry (as $\mathrm{SZA} > 90^\circ$), whose computational cost for a given cloud, aerosol scenario, and wavelength is very high. Moreover, the simulations shown in Fig. 1 indicate that $\mathrm{SZA_{max}}$ depends not only on the cloud altitude but also on the wavelengths employed to compute the CI, preventing the derivation of a unique h_C–$\mathrm{SZA_{max}}$ relation that could be universally applied to instruments such as radiometers or spectrometers observing the twilight intensity. Additionally, the geometry of the problem implies that the cloud layer cannot be modeled as a spherical shell in RT simulations at twilight (Gomez-Martin et al., 2021; Lauster et al., 2022). If the cloud were treated as a spherical shell rather than as a localized layer, then for $\mathrm{SZA} > 90^\circ$ the direct solar radiation would interact twice with the cloud (see Fig. 2). This would imply a cloud layer extending horizontally over several hundred kilometers, which is not realistic and could lead to simulations that do not accurately represent actual atmospheric conditions. Finally, it is important to note that while Monte Carlo RT simulations can be used to retrieve cloud altitudes from zenith intensity observations, it is not straightforward to identify from these simulations how the different atmospheric parameters involved jointly determine $\mathrm{SZA_{max}}$. For these reasons, in the next section we analyze the CI under the single-scattering approximation, introducing a new methodology that provides a clearer understanding of the factors driving the maximum in the CI when high-altitude clouds are present. The goal of this approach is not only to reduce the computational complexity and facilitate the exploration of different atmospheric scenarios, but also to enable a more transparent investigation

https://doi.org/10.5194/egusphere-2026-2295
Preprint. Discussion started: 26 May 2026

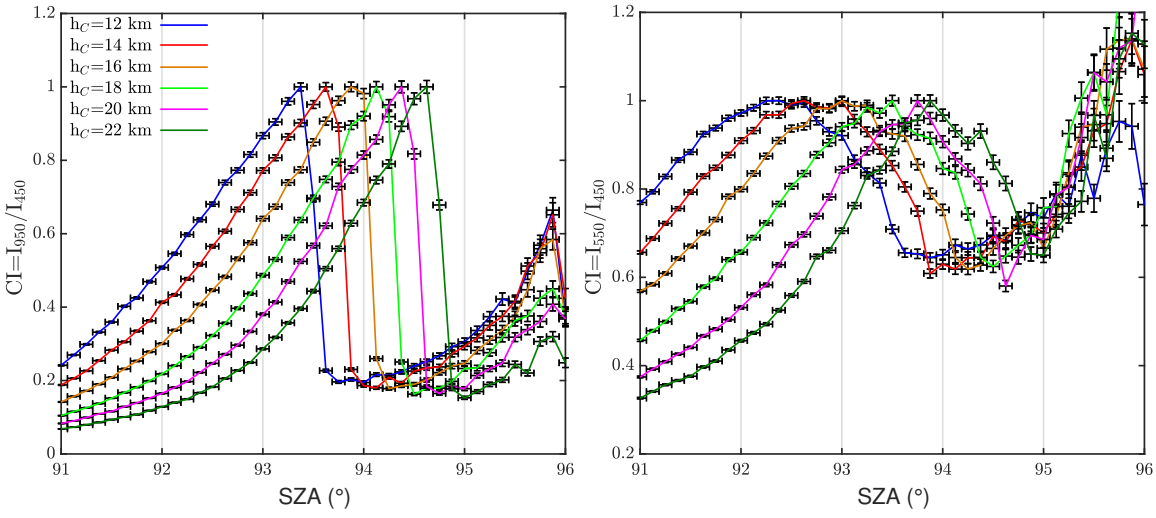

Figure 1. Variation of the CI with SZA for $\lambda_1 = 450$ nm and $\lambda_2 = 950$ nm (left panel), and for $\lambda_1 = 450$ nm and $\lambda_2 = 550$ nm (right panel), as simulated using a Monte Carlo radiative transfer (RT) model for different cloud altitudes ($h_C = 12, 14, 16, 18, 20$, and 22 km). The cloud was the only aerosol included in the simulations, with a geometrical thickness of 2 km in all cases. All CI signals were normalized to their respective maximum values.

of the physical processes governing CI_{max}.

3 Single scattering color index

3.1 Methodology

Instead of solving the RT equation under the single-scattering approximation, we formulate the problem in terms of the probability that an instrument located at the surface and pointing at the zenith detects a photon scattered by a cloud at an altitude h_C during twilight. If we assume that photons undergo at most a single scattering event, then for given values of SZA, h_C, and λ, the probability P that the instrument detects a cloud-scattered photon can be written as:

$$P(\text{SZA}, z = h_C, \lambda) = P_1(\text{SZA}, z = h_C, \lambda) \times P_2^c(\text{SZA}, z = h_C, \lambda) \times P_3(\text{SZA}, z = h_C, \lambda) \quad (2)$$

Here, (i) P_1 represents the probability that a direct solar photon reaches the cloud without being scattered or absorbed along its trajectory from the top of the atmosphere to the cloud (path between points (1) and (2) in Fig. 2a); (ii) P_2^c represents the probability that the cloud scatters the photon toward the instrument, corresponding to a scattering angle equal to the SZA; and (iii) P_3 is the probability that a photon at altitude h_C, traveling downward at a zenith angle of 180°, reaches the instrument without undergoing absorption or additional scattering (path between points (2) and (3) in Fig. 2a). The probabilities P_1 and

https://doi.org/10.5194/egusphere-2026-2295
Preprint. Discussion started: 26 May 2026

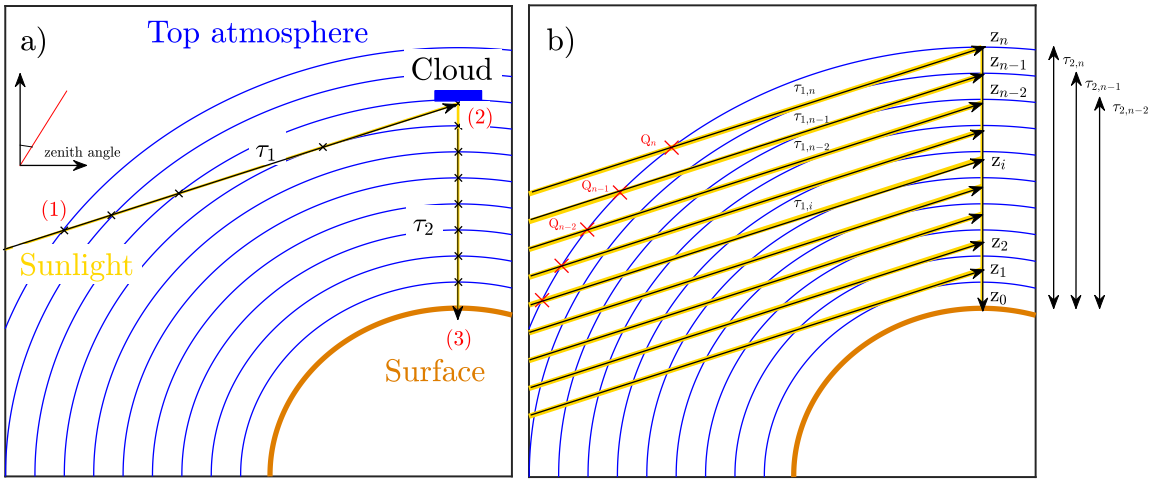

Figure 2. (a) Schematic showing the path followed by a direct solar photon scattered by a cloud at a scattering angle equal to the SZA. Direct light enters the atmosphere at point (1) and propagates to point (2), where it is scattered by the cloud toward the instrument located at point (3). The quantities τ_1 and τ_2 represent the opacity due to molecules and aerosols along segments (1)–(2) and (2)–(3), respectively. (b) Same as panel (a), but for trajectories intersecting the vertical axis at point (3) at different altitudes $(z_1, z_2, \ldots, z_n)$. The points $Q_n, Q_{n-1}, \ldots$ indicate the locations where direct solar radiation enters the atmosphere for the different trajectories.

P_3 are determined by the properties of the background atmosphere at wavelength λ, whereas P_2^c depends solely on the cloud scattering optical depth and phase function. Equation (2) accounts only for photons scattered by the cloud at altitude h_C. Therefore, to reproduce the total zenith intensity measured at the surface, contributions from photons scattered at all altitudes and by molecules or other aerosols present in the atmosphere must be considered. In this case, the total probability of detecting a photon with the instrument (P_{Total}) is obtained by integrating P over altitude (see the right panel of Fig. 2b):

$$P_{\text{Total}}(\lambda, \text{SZA}) = \int_{z_{\text{dark}}}^{z_{\text{top}}} P_1(z, \lambda, \text{SZA}) \times P_2(z, \lambda, \text{SZA}) \times P_3(z, \lambda)\, dz, \tag{3}$$

where P_2 represents the probability that a photon is scattered at altitude z into the zenith line of sight of the instrument, corresponding to a scattering angle $\theta = \text{SZA}$ with respect to the incident solar direction. Note that in Eq. 3, P_2 evaluated at $z = h_C$ accounts for photons scattered by the cloud, molecules, and any other aerosols present at that altitude. If the molecular and aerosol opacities are negligible at h_C, then $P_2(h_C) = P_2^c(h_C)$. Here, z_{top} denotes the altitude of the top of the atmosphere, while z_{dark}, which depends on the SZA, is the altitude at which direct solar radiation is fully blocked by the Earth curvature during twilight, marking the transition above which the atmosphere no longer receives direct illumination. From Eq. 3, we define the single-scattering CI as:

$$\text{CI}^*(\text{SZA}) = \frac{P_{\text{Total}}(\lambda_2, \text{SZA})}{P_{\text{Total}}(\lambda_1, \text{SZA})}, \tag{4}$$

https://doi.org/10.5194/egusphere-2026-2295
Preprint. Discussion started: 26 May 2026

where $\lambda_2 > \lambda_1$. To compute P_{Total}, explicit expressions for P_1, P_2, and P_3 are required. For a given altitude z above the instrument and a given SZA, the probability P_1 can be written as

$$P_1(z,\lambda,\mathrm{SZA}) = \exp[-\tau_1(z,\mathrm{SZA},\lambda)], \tag{5}$$

where $\tau_1(z,\mathrm{SZA},\lambda)$ is the optical depth along the line of sight (see Fig. 2). To estimate $\tau_1(z,\mathrm{SZA},\lambda)$, we assume that aerosol and molecular extinction (S) decrease exponentially with altitude, with scale heights H^{A} and H^{M}, respectively:

$$\begin{aligned} S(z,\lambda) &= S_0^{\mathrm{A}}(\lambda)\exp\Big(-\frac{z}{H^{\mathrm{A}}}\Big) + S_0^{\mathrm{M}}(\lambda)\exp\Big(-\frac{z}{H^{\mathrm{M}}}\Big) \\ &= \frac{\tau_0^{\mathrm{A}}(\lambda)}{H^{\mathrm{A}}}\exp\Big(-\frac{z}{H^{\mathrm{A}}}\Big) + \frac{\tau_0^{\mathrm{M}}(\lambda)}{H^{\mathrm{M}}}\exp\Big(-\frac{z}{H^{\mathrm{M}}}\Big), \end{aligned} \tag{6}$$

where S_0^{A} and S_0^{M} are the aerosol and molecular extinction coefficients at the surface, and τ_0^{A} and τ_0^{M} are the corresponding total aerosol and molecular optical depths. For a given altitude z above the instrument and a given SZA, the optical depth along the line of sight is given by

$$\begin{aligned} \tau_1(z,\mathrm{SZA},\lambda) = S_0^{\mathrm{A}}(\lambda) &\int_0^{l(z,\mathrm{SZA})} \exp\left[-\frac{\sqrt{l'^2+(R_{\mathrm{T}}+z)^2+2l'\mu(R_{\mathrm{T}}+z)}-R_{\mathrm{T}}}{H^{\mathrm{A}}}\right] dl' \\ + S_0^{\mathrm{M}}(\lambda) &\int_0^{l(z,\mathrm{SZA})} \exp\left[-\frac{\sqrt{l'^2+(R_{\mathrm{T}}+z)^2+2l'\mu(R_{\mathrm{T}}+z)}-R_{\mathrm{T}}}{H^{\mathrm{M}}}\right] dl', \end{aligned} \tag{7}$$

where $l(z,\mathrm{SZA})$ is the distance between the point $(0,z)$ and the intersection with the top of the atmosphere (points Q_i in Fig. 2b). To derive Eq. 7, we use the relation $r = \sqrt{l^2+(R_{\mathrm{T}}+z)^2+2l\mu(R_{\mathrm{T}}+z)}$, where r is the radial distance, R_{T} is the planetary radius, and $\mu = \cos(\mathrm{SZA})$. Using trigonometry, the path length $l(z,\mathrm{SZA})$ can be expressed as a function of z and the SZA:

$$l(z,\mathrm{SZA}) = \sqrt{(z_{\mathrm{top}}+R_{\mathrm{T}})^2 + (z+R_{\mathrm{T}})^2\left[\sin^4(\alpha)-\cos^4(\alpha)\right] + 2(z+R_{\mathrm{T}})\sin(\alpha)\sqrt{(z_{\mathrm{top}}+R_{\mathrm{T}})^2-(z+R_{\mathrm{T}})^2\cos^2(\alpha)}}, \tag{8}$$

where $\alpha = \mathrm{SZA} - 90°$. It is important to note that, for the estimation of τ_1, the opacity of the cloud is not included. This is because, in our model, the cloud has a limited horizontal extent and is localized above the instrument, rather than being treated as a spherical shell. The treatment of the cloud horizontal extent, and its impact on P_1, is introduced later in the context of the comparison with the Monte Carlo simulations.

The integrals in Eq. 7 do not admit analytical solutions and must therefore be evaluated numerically. Since the terms S_0^{A} and S_0^{M} are outside the integrals, a precomputed look-up table for the integrals in Eq. 7 as a function of z, SZA, H^{A}, and H^{M} can be constructed. In this case, P_1 can be written as

$$P_1(z,\mathrm{SZA},\lambda) = \exp\left[-\left(J^{\mathrm{A}}(z,\mathrm{SZA},H^{\mathrm{A}})\,S_0^{\mathrm{A}}(\lambda) + J^{\mathrm{M}}(z,\mathrm{SZA},H^{\mathrm{M}})\,S_0^{\mathrm{M}}(\lambda)\right)\right], \tag{9}$$

where J^{A} and J^{M} denote the integrals in Eq. 7, which are precomputed and therefore do not need to be recalculated when the wavelength or the aerosol scenario is changed.

As indicated above, P_2 represents the probability that direct solar radiation reaching an altitude z above the instrument is

https://doi.org/10.5194/egusphere-2026-2295
Preprint. Discussion started: 26 May 2026

scattered at a scattering angle equal to the SZA. Consequently, this probability is proportional to the scattering extinction coefficient at altitude z—including contributions from aerosols, molecules, and clouds—and to the phase function $p(\theta)$ evaluated at $\theta = \mathrm{SZA}$. If the vertical distribution of the cloud is described by a Gaussian height profile, then P_2 can be written as:

$$\begin{aligned} P_2(z,\mathrm{SZA},\lambda) = C\Bigg[& S_0^{\mathrm{A}}(\lambda)\,\omega^{\mathrm{A}}(\lambda)\,\exp\!\left(-\frac{z}{H^{\mathrm{A}}}\right) p^{\mathrm{A}}(\lambda,\mathrm{SZA}) \\ & + S_0^{\mathrm{M}}(\lambda)\,\omega^{\mathrm{M}}(\lambda)\,\exp\!\left(-\frac{z}{H^{\mathrm{M}}}\right) p^{\mathrm{M}}(\lambda,\mathrm{SZA}) \\ & + \frac{\tau^{\mathrm{C}}(\lambda)\,\omega^{\mathrm{C}}(\lambda)}{\Delta h_{\mathrm{C}}}\sqrt{\frac{2}{\pi}}\,\exp\!\left[-\frac{2(z-h_{\mathrm{C}})^2}{\Delta h_{\mathrm{C}}^2}\right] p^{\mathrm{C}}(\lambda,\mathrm{SZA})\Bigg], \end{aligned} \tag{10}$$

where ω^{A}, ω^{M}, and ω^{C} are the aerosol, molecular, and cloud single-scattering albedos, respectively; p^{A}, p^{M}, and p^{C} are the corresponding phase functions; τ^{C} and Δh_{C} are the cloud total optical depth and geometrical thickness; and C is a normalization constant that, as shown below, does not need to be explicitly evaluated in our analysis. In Eq. 10, the only term depending explicitly on the SZA is the phase function. However, given the limited SZA range considered here, the impact of phase-function variations on $\mathrm{SZA}_{\mathrm{max}}$ is expected to be small.

The last term to be computed is $P_3(z,\lambda)$, which represents the probability that a photon travels vertically from altitude z to the surface without undergoing absorption or scattering. This probability is given by

$$P_3(z,\lambda) = \exp[-\tau_2(z,\lambda)], \tag{11}$$

where $\tau_2(z,\lambda)$ is the optical depth due to aerosols, molecules, and clouds between altitude z and the surface (see Fig. 2), and is computed as

$$\begin{aligned} \tau_2(z,\lambda) = {} & \tau_0^{\mathrm{A}}\left(1-\exp\!\left[-\frac{z}{H^{\mathrm{A}}}\right]\right) + \tau_0^{\mathrm{M}}\left(1-\exp\!\left[-\frac{z}{H^{\mathrm{M}}}\right]\right) \\ & + \frac{\tau_{\mathrm{C}}}{2}\left[\mathrm{erf}\left(\sqrt{2}\,\frac{z-h_{\mathrm{C}}}{\Delta h_{\mathrm{C}}}\right) - \mathrm{erf}\left(-\sqrt{2}\,\frac{h_{\mathrm{C}}}{\Delta h_{\mathrm{C}}}\right)\right]. \end{aligned} \tag{12}$$

Here, erf denotes the error function, defined as

$$\mathrm{erf}(x) = \frac{2}{\sqrt{\pi}}\int_0^x e^{-t^2}\,dt. \tag{13}$$

Once P_1, P_2, and P_3 are defined, the total probability P_{Total} is obtained by integrating their product from z_{dark} to the top of the atmosphere. Scripts to compute P_1, P_2, P_3, and P_{Total} are publicly available at (Toledo, 2026).

In the following sections, we first analyze the behavior of P_1, P_2, and P_3, and their contribution to P_{Total}, in order to study the properties of the CI as a function of cloud altitude and wavelengths. We then show that the single-scattering CI^* reproduces the main features of the CI obtained from full Monte Carlo RT simulations.

https://doi.org/10.5194/egusphere-2026-2295
Preprint. Discussion started: 26 May 2026

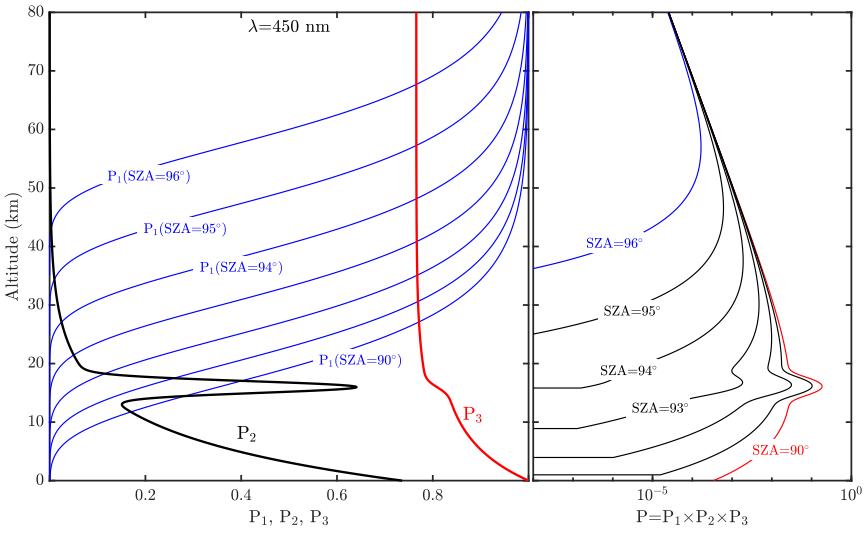

Figure 3. Variation of P_1, P_2, P_3, and P with altitude at 450 nm for different SZAs (90°, 91°, 92°, 93°, 94°, 95°, and 96°), considering a cloud layer located at an altitude of 16 km, with a geometrical thickness of 2 km and a total optical depth of 0.05. The P_2 curves (left panel) were normalized by P_{Total} at SZA $= 90°$.

3.2 Simulation of P_1, P_2, P_3, P_{Total} and CI*

Figures 3 and 4 show the variation of P_1, P_2, P_3, and P_{Total} with altitude at 450 and 950 nm for different SZAs, considering a cloud layer located at an altitude of 16 km. In these simulations, the phase functions were omitted in the computation of P_2, and both ω^{M} and ω^{C} were set to unity. The P_2 curves were normalized by P_{Total} at SZA $= 90°$. As discussed below, for a given cloud scenario, the choice of normalization in Eq. 10 does not affect the value of $\mathrm{SZA}_{\mathrm{max}}$ derived from the model. As shown in Figs. 3 and 4, P_1 increases with altitude and decreases with SZA as a consequence of the dependence of τ_1 (Eq. 7) on these parameters. For a given altitude z above the surface, the path segment between points Q and $(0, z)$ intersects progressively lower atmospheric layers as the SZA increases, where the molecular opacity is higher, leading to larger values of τ_1. For fixed values of SZA and z, P_1 is also larger at 950 nm than at 450 nm, reflecting the decrease of Rayleigh opacity with increasing wavelength. At 450 nm (Fig. 3) and for SZA $\gtrsim 93°$, most of the photons reaching the instrument originate from scattering events occurring at altitudes above the cloud layer, as indicated by the behavior of P in Fig. 3. The altitude at which direct solar radiation is completely blocked by the Earth curvature is given by

$$z_{\mathrm{dark}} = R_{\mathrm{T}} \left(\sqrt{1 + \tan^2(\alpha)} - 1 \right), \tag{14}$$

Thus, for SZA $= 93°$ and $94°$, z_{dark} is 8.7 km and 15.5 km, respectively, which are both below the altitude of maximum cloud opacity ($h_{\mathrm{C}} = 16$ km). This indicates that, at 450 nm, and as a result of molecular opacity, the cloud is already effectively in darkness before the surface blocks direct solar radiation at the cloud altitude (SZA $> 94°$). In contrast, at 950 nm (Fig. 4) ,

https://doi.org/10.5194/egusphere-2026-2295
Preprint. Discussion started: 26 May 2026

and for $z_{\mathrm{dark}} < h_{\mathrm{C}}$, the maximum in P occurs at the cloud altitude (for SZA $= 93°$ and $94°$). Therefore, depending on the wavelength, the cloud can enter the dark region of the atmosphere even when $h_{\mathrm{C}} > z_{\mathrm{dark}}$. As discussed below, this behavior is one of the primary factors responsible for the emergence of a maximum in the CI in the presence of high-altitude clouds. With regard to P_2 and P_3, larger values of P_2 are obtained at 450 nm than at 950 nm as a consequence of the stronger molecular opacity at shorter wavelengths. However, since P_1 decreases much more rapidly at 450 nm than at 950 nm for altitudes above z_{dark}, and because P_3 is larger at 950 nm than at 450 nm, the resulting values of P are greater at 950 nm for altitudes near the cloud layer (i.e., for $z > z_{\mathrm{dark}}$).

These results are further illustrated in Fig. 5a, where the P profiles at 450 and 950 nm are compared for three different SZA

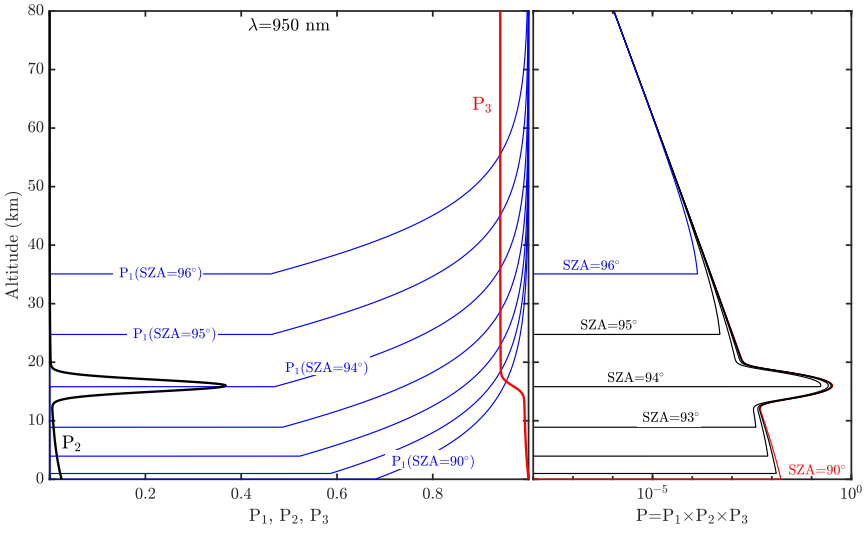

Figure 4. Same as Fig. 3, but at 950 nm.

values. The horizontal black dashed lines indicate the altitude z_{dark} corresponding to each SZA. When SZA $\sim 90°$, the dominant contribution of photons at both wavelengths originates from altitudes around the cloud layer. However, as the SZA increases, the contribution from these altitudes decreases more rapidly at 450 nm than at 950 nm. As a result, P_{Total} decreases more slowly with increasing SZA at 950 nm than at 450 nm, and it is precisely this effect that causes CI* to increase over this SZA range, as shown in Fig. 5b. The increase in CI* continues up to SZA $\sim 93.8°$, beyond which CI* decreases rapidly with SZA. By comparing the P profiles with the CI* signal in Fig. 5, we see that this transition occurs close to the moment when the cloud begins to darken at 950 nm. These results indicate that the maximum in CI* occurs at larger SZA values as λ_2 increases, since lower molecular opacity delays the onset of cloud darkening. In the limiting case where the molecular opacity at λ_2 is negligible, $\mathrm{SZA}_{\mathrm{max}}$ approaches $\mathrm{SZA}_{\mathrm{dark}}$, which can be obtained from Eq. 14 by setting $z = h_{\mathrm{C}}$. For the example shown in Fig. 5, $\mathrm{SZA}_{\mathrm{dark}} = 94.06°$, which is close to the corresponding value of $\mathrm{SZA}_{\mathrm{max}}$. From this, we conclude that for a given

https://doi.org/10.5194/egusphere-2026-2295
Preprint. Discussion started: 26 May 2026

$\mathrm{SZA}_{\max}$, the cloud altitude must satisfy

$$h_{\mathrm{C}} \geq R_{\mathrm{T}} \left(\sqrt{1 + \tan^2(\mathrm{SZA}_{\max} - 90^\circ)} - 1 \right). \quad (15)$$

If an increase in λ_2 results in an increase in the value of $\mathrm{SZA}_{\max}$, the next point to address is the dependence of $\mathrm{SZA}_{\max}$ on

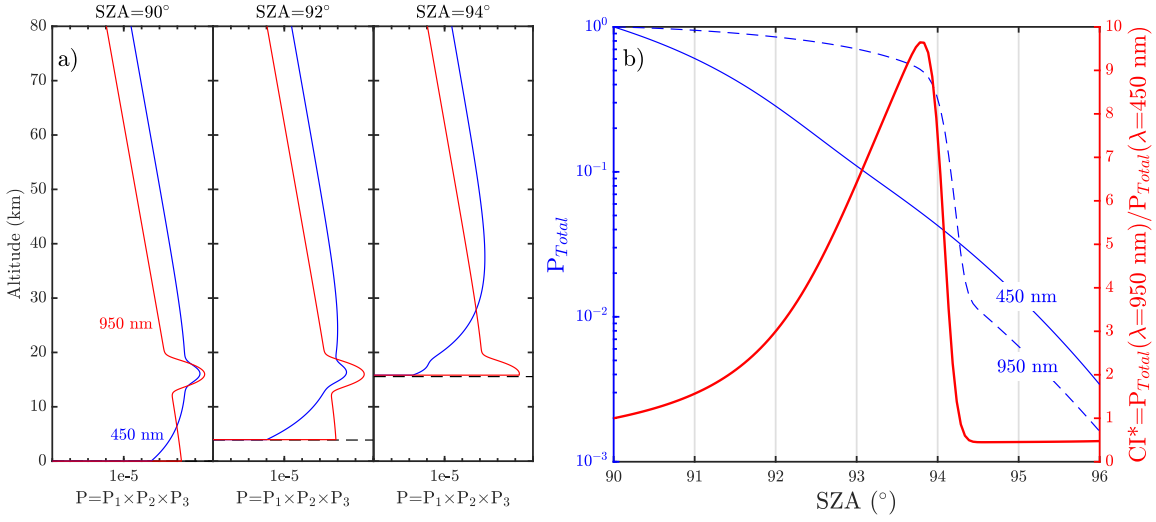

Figure 5. (a) Vertical profiles of P at 450 nm (blue lines) and 950 nm (red lines) for SZA $= 90^\circ$, 92°, and 94°. The atmospheric scenario is the same as in Figs. 3 and 4. (b) Variation of P_{Total} at 450 nm (blue solid line) and 950 nm (blue dashed line) with SZA for the atmospheric conditions of Figs. 3 and 4. The red solid line represents CI^* obtained from P_{Total} at 450 and 950 nm.

λ_1 for a fixed λ_2. We performed simulations similar to those shown in Fig. 5 for different values of λ_1 and found almost no variation in $\mathrm{SZA}_{\max}$ when λ_1 ranges between 400 and 500 nm while λ_2 is fixed at 950 nm. Although the shape of the CI^* signal changes, the value of $\mathrm{SZA}_{\max}$ remains nearly unchanged. However, for larger values of λ_1, a noticeable shift in $\mathrm{SZA}_{\max}$ is observed. In the following section, we further investigate how variations in λ_1 influence $\mathrm{CI}_{\max}$.

3.3 Origin of the wavelength dependence of the CI^* maximum

To study the dependence of $\mathrm{SZA}_{\max}$ on λ_1 and λ_2 for a given cloud scenario, we examine the condition defining the maximum of CI^*. This can be obtained by computing the derivative of CI^* with respect to the SZA and setting it equal to zero. Under this condition, $\mathrm{SZA}_{\max}$ satisfies:

$$\frac{1}{P_{\mathrm{Total}}(\lambda_1, \mathrm{SZA})} \frac{\partial P_{\mathrm{Total}}(\lambda_1, \mathrm{SZA})}{\partial \mathrm{SZA}} = \frac{1}{P_{\mathrm{Total}}(\lambda_2, \mathrm{SZA})} \frac{\partial P_{\mathrm{Total}}(\lambda_2, \mathrm{SZA})}{\partial \mathrm{SZA}} \quad (16)$$

Equation (16) shows that the CI^* maximum occurs at the SZA for which both wavelengths exhibit identical relative SZA-variations of P_{Total}. In other words, the maximum does not arise only from the cloud contribution, but from the differential evolution of the zenith intensity with SZA at the two selected wavelengths. Equation (16) also indicates that any multiplicative

https://doi.org/10.5194/egusphere-2026-2295
Preprint. Discussion started: 26 May 2026

constant applied to P_{Total} in Eq. 3, such as a normalization factor, does not modify the value of $\mathrm{SZA}_{\mathrm{max}}$.

As an example, Figure 6a shows the relative rate of variation of $P_{\mathrm{Total}}(\lambda, \mathrm{SZA})$ with respect to SZA at different wavelengths for the same cloud scenario as in Figs. 3 and 4. Figure 6b shows the corresponding CI^* signals for the same cloud scenario and wavelength combinations as in Figure 6a, with $\lambda_1 = 400$ nm fixed and λ_2 varying. As expected, $\mathrm{SZA}_{\mathrm{max}}$ coincides with the SZA at which the relative SZA-variation curves of P_{Total} intersect. In the previous section, we indicated that simulations similar to those shown in Fig. 5, but considering λ_1 values between 400 and 500 nm while keeping $\lambda_2 = 950$ nm fixed, exhibit no significant variations in $\mathrm{SZA}_{\mathrm{max}}$. This behaviour is readily understood from the relative SZA-variation curves of P_{Total}, where the curves corresponding to 400 and 500 nm are nearly indistinguishable for $\mathrm{SZA} \gtrsim 93.5°$. As a result, their intersection with the $\lambda_2 = 950$ nm curve occurs at essentially the same SZA, leading to nearly identical values of $\mathrm{SZA}_{\mathrm{max}}$. However, if instead of using $\lambda_2 = 950$ nm we consider $\lambda_2 \lesssim 700$ nm, noticeable variations in $\mathrm{SZA}_{\mathrm{max}}$ may arise when λ_1 is varied between 400 and 500 nm.

In Figure 6a we also see that, as λ_2 increases relative to 400 nm, the intersection between the corresponding relative SZA-variation curves becomes progressively more transversal, which corresponds to a larger difference between their local slopes at the crossing point. As a consequence, the curvature of CI^* around $\mathrm{SZA}_{\mathrm{max}}$ increases, leading to a more pronounced and better-defined maximum in Figure 6b. Conversely, when the relative variation curves intersect with nearly parallel slopes, the resulting CI^* maximum is broader and less pronounced. This aspect is particularly relevant for real zenith radiance measurements, where instrumental noise and atmospheric variability introduce uncertainties in the determination of $\mathrm{SZA}_{\mathrm{max}}$. A sharper maximum enhances the robustness of cloud detection and improves the precision in the inferred cloud altitude.

Although these results suggest that increasing the spectral separation between λ_1 and λ_2 generally leads to a sharper CI^* maximum and therefore to potentially more precise determinations of $\mathrm{SZA}_{\mathrm{max}}$, the situation is more complex in practice. The shape of the relative SZA-variation curves of P_{Total} also depend on the cloud altitude and on the overall atmospheric optical properties. Consequently, identifying an optimal combination of λ_1 and λ_2 that minimizes the uncertainty in the retrieved cloud height is not straightforward. In the following section, we introduce an alternative CI-based index specifically designed to improve the robustness of twilight cloud-height estimation.

3.4 Spectral selection constraints and development of a Rayleigh-based CI

In the previous section, we highlighted the difficulty of identifying a globally optimal combination of λ_1 and λ_2 even under the simplified assumption of a single cloud layer and molecular scattering only. In realistic atmospheric conditions, however, additional components such as aerosol layers or absorbing gases further increase the complexity of twilight RT. An example is the analysis of CI at wavelengths where the absorption of NO_2 or O_3 is significant (Gomez-Martin et al., 2021). In such cases, the presence of an absorbing layer modifies the total optical depth and therefore affects P_{Total}. Consequently, its contribution must be explicitly incorporated into the analysis. The absorption opacity due to gases can be directly included in Eqs. 7 and 12 if vertical profiles are available, or alternatively parametrized using a Gaussian profile similar to that adopted for the cloud layer. Assuming a Gaussian-type parametrization, the contribution to P_1 requires a term analogous to J^{A} and J^{M}, following the same

https://doi.org/10.5194/egusphere-2026-2295
Preprint. Discussion started: 26 May 2026

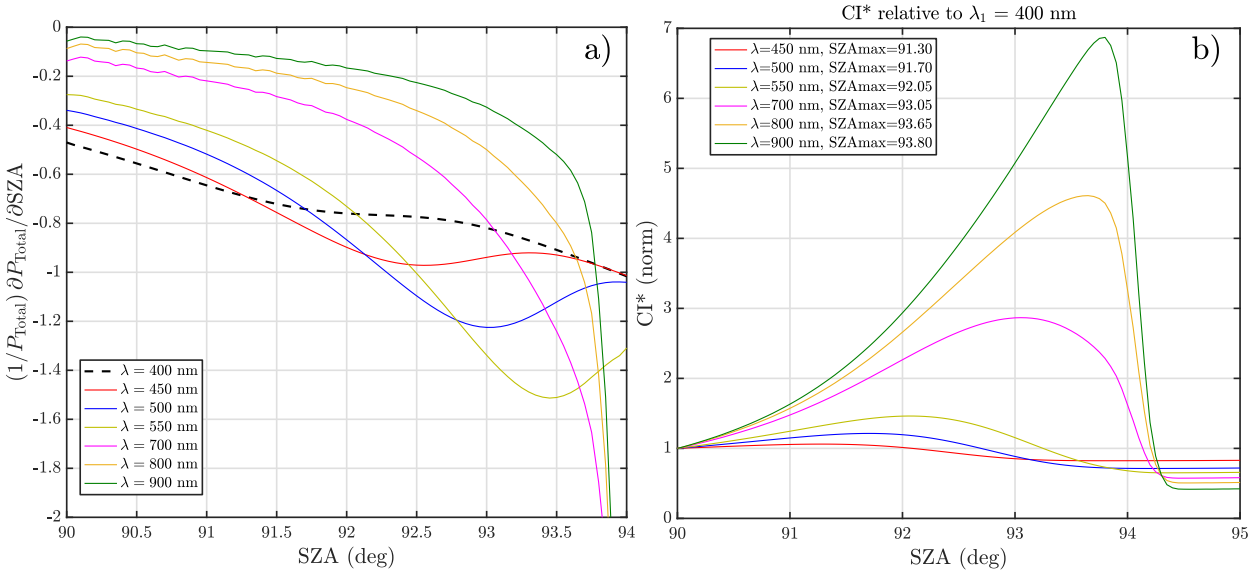

Figure 6. Variation of $\left(\frac{1}{P_{\mathrm{Total}}(\lambda,\mathrm{SZA})} \cdot \frac{\partial P_{\mathrm{Total}}(\lambda,\mathrm{SZA})}{\partial \mathrm{SZA}}\right)$ with SZA at 400, 450, 500, and 950 nm for the atmospheric conditions of Figs. 3 and 4. Panel (b) shows the corresponding CI* signals for the same atmospheric conditions as in panel a, with $\lambda_1 = 400$ nm fixed and $\lambda_2 = 450$, 500, 550, 700, 800, and 900 nm.

procedure used in Eq. 7 but with a Gaussian dependence on z. For the calculation of P_3 through τ_2, the absorption opacity of gases (τ^{Abs}) can be incorporated into Eq. 12 through

$$\tau^{\mathrm{Abs}}(z,\lambda) = \frac{\tau^{\mathrm{Total}}_{\mathrm{Abs}}}{2}\left[\mathrm{erf}\left(\sqrt{2}\,\frac{z-h_{\mathrm{Abs}}}{\Delta h_{\mathrm{Abs}}}\right) - \mathrm{erf}\left(-\sqrt{2}\,\frac{h_{\mathrm{Abs}}}{\Delta h_{\mathrm{Abs}}}\right)\right], \tag{17}$$

where $\tau^{\mathrm{Total}}_{\mathrm{Abs}}$, h_{Abs}, and Δh_{Abs} denote the total optical depth, central altitude, and geometrical thickness of the absorbing layer, respectively.

However, in many cases these gases exhibit a pronounced seasonal variability in both their vertical distribution and total column abundance (see, e.g., (Gomez-Martin et al., 2021)), and an inaccurate representation of such temporal cycles may lead to significant errors in the retrieved cloud altitude. This introduces an additional temporal dependence in the RT simulations. In such cases, an alternative approach is to select λ_1 and λ_2 outside the main absorption bands of the gases present, thereby simplifying the RT modelling. However, this criterion — avoiding absorption bands while simultaneously maximizing the spectral separation between λ_1 and λ_2 in order to enhance the robustness of the retrieval — is not always feasible in practice. Figure 7 illustrates this limitation by showing the absorption cross sections of NO_2 (green) and O_3 (blue), derived from Burrows et al. (1998) and Molina and Molina (1986). The spectral bands selected in previous CI-based retrieval studies are also indicated for reference. In Figure 6 we saw that a suitable choice for λ_1 is around 400 nm, since the cloud signature at this wavelength is less pronounced than at longer wavelengths, which leads to a more pronounced CI* maximum. Figure 7 shows that selecting λ_1 in the blue spectral region is problematic due to the significant absorption of NO_2 in this range. Although one could shift λ_1

https://doi.org/10.5194/egusphere-2026-2295
Preprint. Discussion started: 26 May 2026

towards 500–550 nm to reduce this effect, such a displacement would require a corresponding shift in λ_2 in order to preserve sufficient spectral separation. This would extend the required spectral range beyond the capabilities of many instruments. For instance, Gomez-Martin et al. (2021) employed measurements from a twin (UV/Vis) Multi-Axis Differential Optical Absorption Spectroscopy (MAX-DOAS) system covering the spectral range from 415 to 542 nm, which limits the available wavelength combinations for CI-based retrievals.

The objective of this section is to define a new CI formulation that enables the detection of clouds during twilight and the

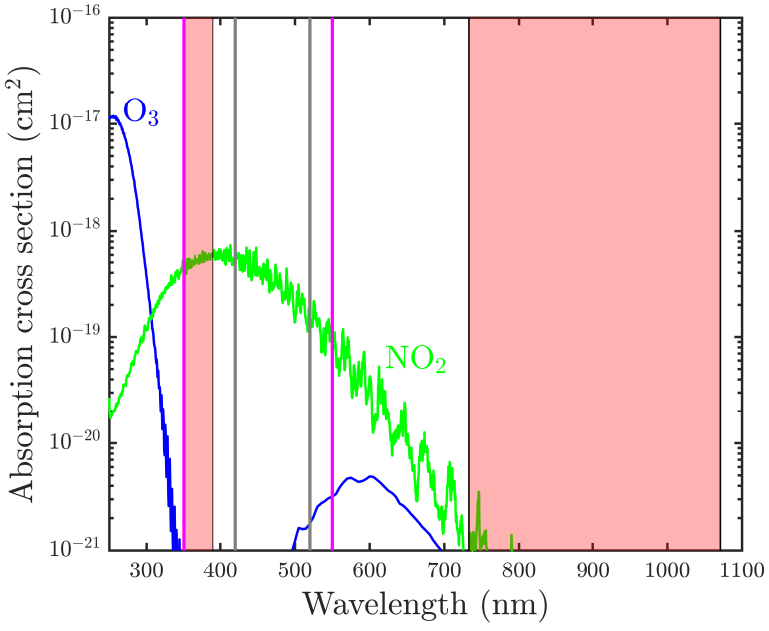

Figure 7. Absorption cross section of NO_2 (green) and O_3 (blue) from Burrows et al. (1998) and Molina and Molina (1986), respectively. The gray and purple vertical lines represent the wavelengths selected in Gomez-Martin et al. (2021) and Sarkissian et al. (1991) to compute the CI, respectively, while the red blocks indicate the wavelength ranges used in Toledo et al. (2016).

estimation of their altitude, while avoiding the need to select λ_1 in spectral regions that are problematic for RT simulations. As shown in Figures 3 and 7, when $\lambda_1 = 400$ nm (or similar) is employed, the CI* maximum occurs at an SZA at which the cloud is already completely in shadow. Thus, at λ_1 and for SZA values around or larger than $\mathrm{SZA}_{\max}$, P_{Total} does not differ significantly from that expected in a purely Rayleigh-scattering atmosphere. Indeed, Figures 8a and 8b show the relative SZA-variation curves $\frac{1}{P_{\mathrm{Total}}(\lambda,\mathrm{SZA})}\frac{\partial P_{\mathrm{Total}}(\lambda,\mathrm{SZA})}{\partial \mathrm{SZA}}$ for both the cloud+Rayleigh scenario and the pure Rayleigh case at 400, 700, and 900 nm. In these cases, it can be seen that the relative variations in the pure Rayleigh atmosphere closely resemble those of the cloud+Rayleigh case at 400 nm in the vicinity of the intersection of the curves that determines $\mathrm{SZA}_{\max}$. From this reasoning, we define a Rayleigh-referenced color index, CI^R, as

$$\mathrm{CI}^R(\mathrm{SZA}) = \frac{P_{\mathrm{Total}}(\lambda,\mathrm{SZA})}{P^R_{\mathrm{Total}}(\lambda,\mathrm{SZA})}, \tag{18}$$

https://doi.org/10.5194/egusphere-2026-2295
Preprint. Discussion started: 26 May 2026

where $P^{R}_{\mathrm{Total}}(\lambda, \mathrm{SZA})$ denotes the total signal simulated (or measured, if radiances are used) under purely Rayleigh-scattering conditions at wavelength λ. The principle of cloud detection using Eq. 18 is analogous to that of CI^{*}, but with the advantage that it requires observations at only a single wavelength. This allows its application to instruments operating at a single wavelength (or within a narrow spectral band that does not permit the selection of two widely separated wavelengths), thereby simplifying the choice of spectral regions where the observations are less affected by gas absorption. Moreover, provided that the molecular scale height and background atmospheric composition remain stable over time, the SZA dependence of the twilight intensity at a given wavelength in a purely Rayleigh atmosphere is expected to be nearly invariant. Therefore, the same Rayleigh reference signal can be used for the calculation of CI. To show this, Figure 8c illustrates CI^{*} computed for $\lambda_1 = 400$ nm and $\lambda_2 = 700$ and 900 nm, together with CI^{R} calculated at $\lambda = 700$ and 900 nm for the same cloud scenario as in Figure 6. These results clearly demonstrate that, despite being a considerably simpler index, CI^{R} effectively captures the presence of high-altitude clouds during twilight and enables their height to be estimated through RT simulations at a single wavelength.

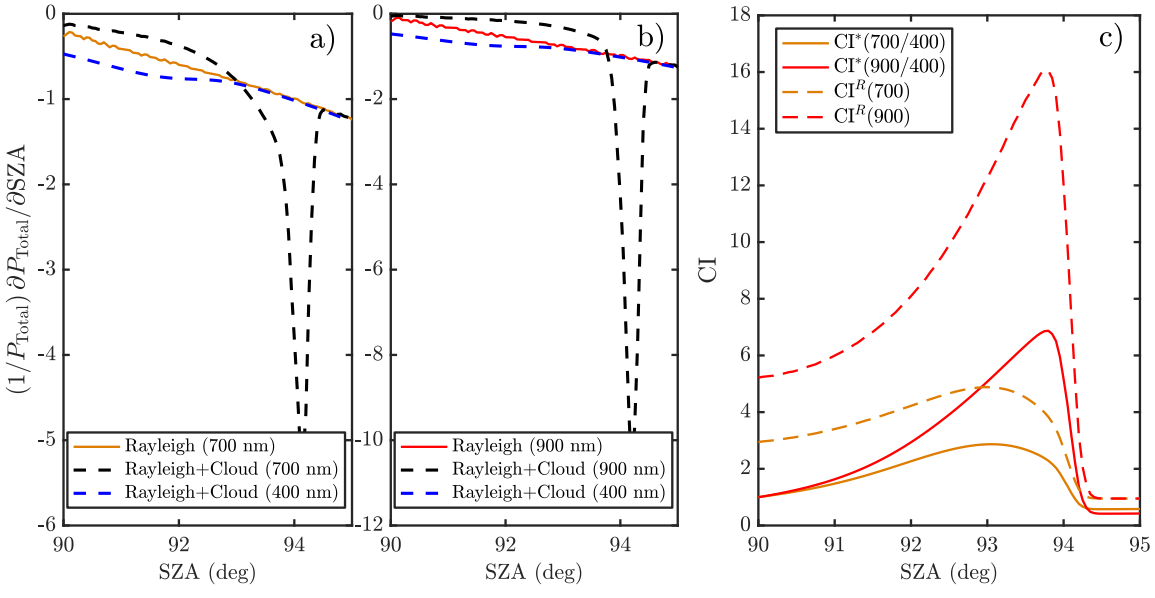

Figure 8. (a) Variation of $\left(\frac{1}{P_{\mathrm{Total}}(\lambda,\mathrm{SZA})} \cdot \frac{\partial P_{\mathrm{Total}}(\lambda,\mathrm{SZA})}{\partial \mathrm{SZA}}\right)$ with SZA for a purely Rayleigh atmosphere at 700 nm, and for an atmosphere including Rayleigh scattering and a cloud layer at 16 km (as in Figure 6) at 400 and 700 nm. Panel (b) shows the same comparison as panel (a), but for 900 nm instead of 700 nm. Panel (c) compares CI^{*} and CI^{R} for the same cloud scenario as in panels (a) and (b). For CI^{*}, $\lambda_1 = 400$ nm and $\lambda_2 = 700$ and 900 nm are used, while CI^{R} is computed at $\lambda = 700$ and 900 nm.

https://doi.org/10.5194/egusphere-2026-2295
Preprint. Discussion started: 26 May 2026

3.5 Comparison against Monte-Carlo simulations

The analyses presented in the previous sections have allowed us to identify the key processes controlling the behaviour of the CI and have led to the definition of a new index, the Rayleigh-referenced color index, CI^R, which may offer practical advantages over the traditional CI based on measurements at two wavelengths. However, it remains necessary to assess how well the single-scattering formulation reproduces the results obtained from a multiple-scattering model in spherical geometry through a comparison of the simulated zenith intensity at twilight. For this purpose, we employ the Monte Carlo model used for the simulations shown in Fig. 1. In order to improve the consistency of the comparison, the vertical and horizontal structure of the cloud is the same in both models. The cloud is assumed to follow a Gaussian distribution not only in the vertical, as described in Eq. 10, but also in the horizontal direction. In this formulation, the cloud extinction coefficient decreases with the horizontal distance from the observer zenith according to:

$$\beta^{\mathrm{C}}(z,\rho,\lambda) = \frac{\tau^{\mathrm{C}}(\lambda)}{\Delta h_{\mathrm{C}}}\sqrt{\frac{2}{\pi}}\exp\left[-\frac{2(z-h_{\mathrm{C}})^2}{\Delta h_{\mathrm{C}}^2}\right]\exp\left[-\frac{\rho^2}{2\,R_{\mathrm{C}}^2}\right], \tag{19}$$

where R_{C} defines the horizontal extent of the cloud and ρ is the horizontal distance from the local vertical axis of the observer. The horizontal distance is approximated as $\rho(l) = r(l)\,\zeta(l)$, where $r(l)$ is the radial distance along the solar path and $\zeta(l)$ is the angular deviation from the local vertical. Here, l denotes the path length along the solar trajectory, as defined in Eq. 8. For clarity, the dependence of l on z and SZA has been omitted in the notation. The angular deviation $\zeta(l)$ is obtained from the spherical geometry of the solar path as:

$$\zeta(l) = \arccos\left(\frac{R_T + z + l\cos(\mathrm{SZA})}{r(l)}\right) = \arccos\left(\frac{R_T + z + l\cos(\mathrm{SZA})}{\sqrt{l^2 + (R_T+z)^2 + 2l\cos(\mathrm{SZA})(R_T+z)}}\right). \tag{20}$$

Note that both P_2 and P_3 are evaluated along the vertical direction of the observer (i.e., at $\rho = 0$). As a result, the horizontal Gaussian distribution does not affect these terms, since the cloud extinction reaches its maximum along the symmetry axis. In contrast, the horizontal structure of the cloud directly impacts the computation of P_1, as the incoming solar radiation propagates along a slanted path and samples regions with $\rho \neq 0$. However, since this contribution enters as an additional extinction term, it can be naturally incorporated into the computation of P_1 by including it in the optical depth integral defined in Eq. 7:

$$P_1(z,\mathrm{SZA},\lambda) = \exp\left[-\left(J^{\mathrm{A}}(z,\mathrm{SZA},H^{\mathrm{A}})\,S_0^{\mathrm{A}}(\lambda) + J^{\mathrm{M}}(z,\mathrm{SZA},H^{\mathrm{M}})\,S_0^{\mathrm{M}}(\lambda) + \int_0^{l(z,\mathrm{SZA})} \beta^{\mathrm{C}}\big(z(l'),\rho(l'),\lambda\big)\,dl'\right)\right], \tag{21}$$

Figures 9a–e show simulations of the variation of the normalized intensity with SZA obtained using the Monte Carlo RT model and the single-scattering approach described in Section 3.1, for a cloud layer with $\tau^{\mathrm{C}} = 0.05$ and $h_{\mathrm{C}} = 12$, 14, 16, 18 and 20 km. For all simulations, the wavelength was fixed at $\lambda = 700$ nm, the horizontal scale at $R_{\mathrm{C}} = 20$ km, and the cloud thickness at $\Delta h_{\mathrm{C}} = 2$ km. The Monte Carlo simulations are limited to $\mathrm{SZA} = 95°$ due to the increased computational cost associated with the adopted cloud geometry. In contrast to spherically symmetric cloud layers, the horizontally localized cloud considered here breaks the symmetry between SZA and latitude, requiring independent simulations for each SZA. This range nevertheless fully covers the region of interest, since the $\mathrm{SZA}_{\mathrm{max}}$ for each simulated cloud height occurs at lower SZA<95°, as indicated by the

https://doi.org/10.5194/egusphere-2026-2295
Preprint. Discussion started: 26 May 2026

dashed black line.

The comparison shown in Fig. 9 demonstrates that the single-scattering model (hereafter SSM) reproduces the Monte Carlo

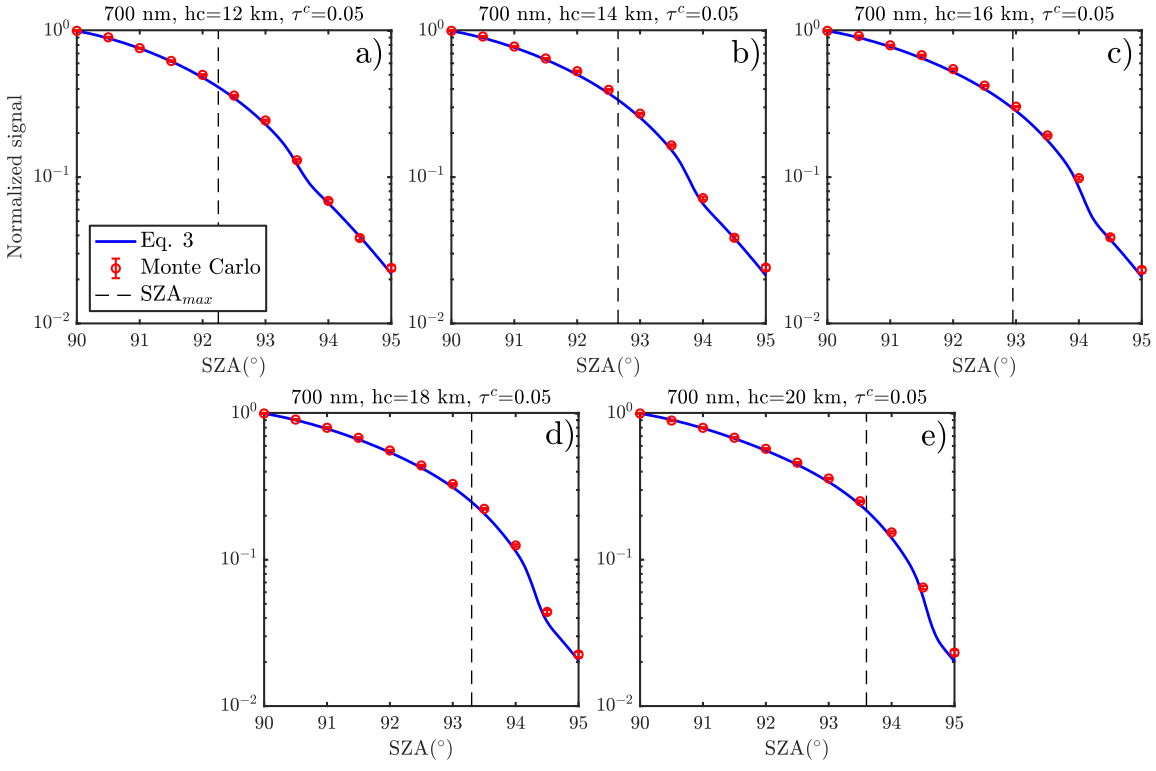

Figure 9. Normalized zenith intensity as a function of SZA for different cloud heights: $h_C = 12$ km (panel a), 14 km (panel b), 16 km (panel c), 18 km (panel d), and 20 km (panel e). All simulations were performed at 700 nm, with cloud optical thickness $\tau_C = 0.05$, horizontal scale $R_C = 20$ km, and cloud geometrical thickness $\Delta h_C = 2$ km. Monte Carlo simulations are shown as red dots, while the single-scattering model is represented by the blue solid lines. The black dashed line indicates the value of $\mathrm{SZA_{max}}$ corresponding to each cloud scenario.

simulations with very good agreement across the full range of cloud altitudes considered. Small differences between both approaches can be observed at larger SZAs (typically above $\sim 94°$), where the deviations slightly increase. However, the SZAs relevant for the determination of the CI maximum occur at lower values, as indicated by the dashed black line marking $\mathrm{SZA_{max}}$ in each panel. Therefore, within the range of interest, the approximations adopted in the SSM remain well within acceptable limits. These results not only support the validity of the formulation developed in the previous sections for investigating the physical origin of the CI maximum, but also demonstrate that the SSM provides a reliable and computationally efficient alternative for the analysis of observational data.

Figure 10 shows a comparison similar to that presented in Fig. 9, but in this case varying the wavelength from 400 to 800 nm in steps of 100 nm, while keeping the cloud height fixed at $h_C = 16$ km. The remaining parameters are kept identical to those used

https://doi.org/10.5194/egusphere-2026-2295
Preprint. Discussion started: 26 May 2026

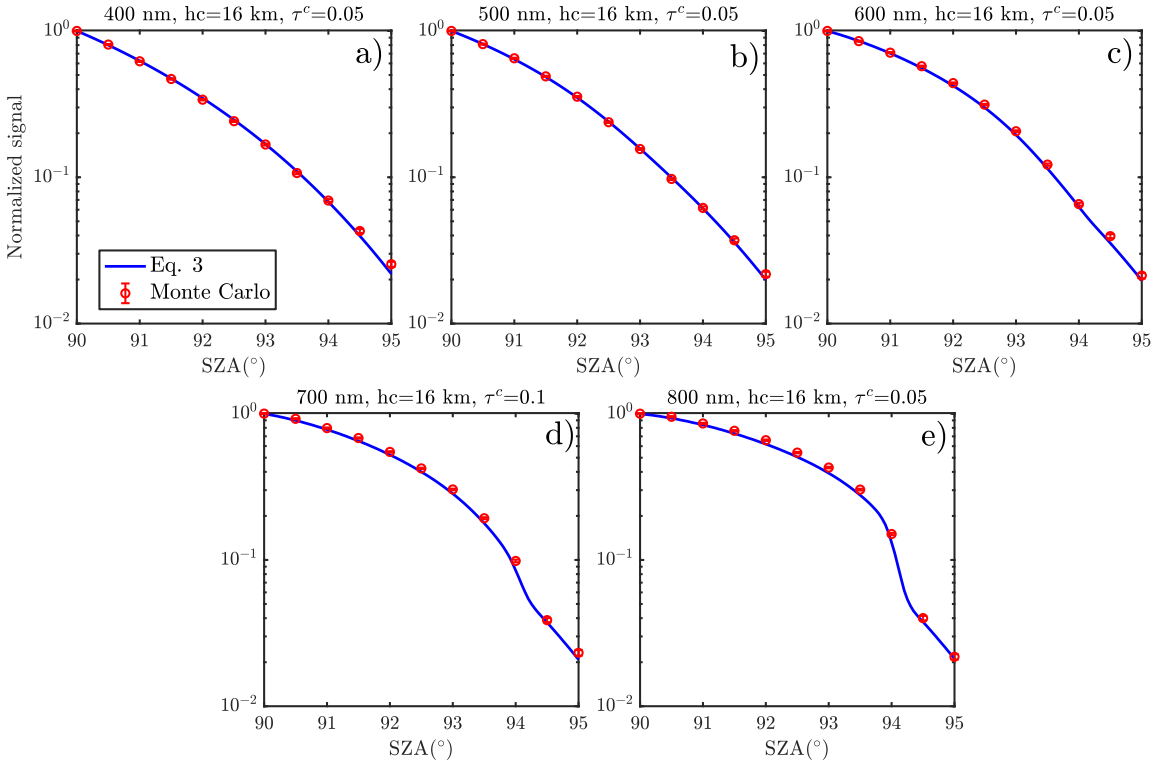

Figure 10. Similar simulations to those shown in Fig. 9, but keeping the cloud height fixed at $h_C = 16$ km and varying the wavelength: 400 nm (panel a), 500 nm (panel b), 600 nm (panel c), 700 nm (panel d), and 800 nm (panel e). The remaining parameters are kept identical to those in Fig. 9.

in Fig. 9. In this scenario, the main wavelength-dependent contribution in the model arises from Rayleigh scattering, whose optical depth varies strongly with wavelength. As a result, the attenuation of the signal along the solar path changes accordingly, while the cloud contribution remains unchanged. This behaviour is clearly reflected in the curves, where the cloud-related feature becomes more pronounced as the wavelength increases. This is consistent with the decreasing contribution of Rayleigh scattering at longer wavelengths, which enhances the relative impact of the cloud on the observed signal. As in the comparison shown in Fig. 9, the SSM reproduces the Monte Carlo simulations with very good agreement across all wavelengths. In particular, the change in the structure of the cloud-induced feature in the intensity profiles is accurately captured by the SSM. Therefore, we conclude that the main findings derived from the comparison in Fig. 9 can be consistently extended to different wavelengths.

Finally, a similar comparison was performed by varying the cloud optical depth from $\tau^C = 0$ (pure Rayleigh atmosphere) up to $\tau^C = 0.3$, as shown in Fig. 11. In all simulations, the cloud height is fixed at $h_C = 16$ km and the wavelength at $\lambda = 700$ nm, while the remaining parameters are kept identical to those used in Fig. 9. The lowest non-zero value considered for the cloud optical depth was $\tau^C = 0.01$. As discussed in the context of Fig. 10, the impact of the cloud is expected to be more pronounced

https://doi.org/10.5194/egusphere-2026-2295
Preprint. Discussion started: 26 May 2026

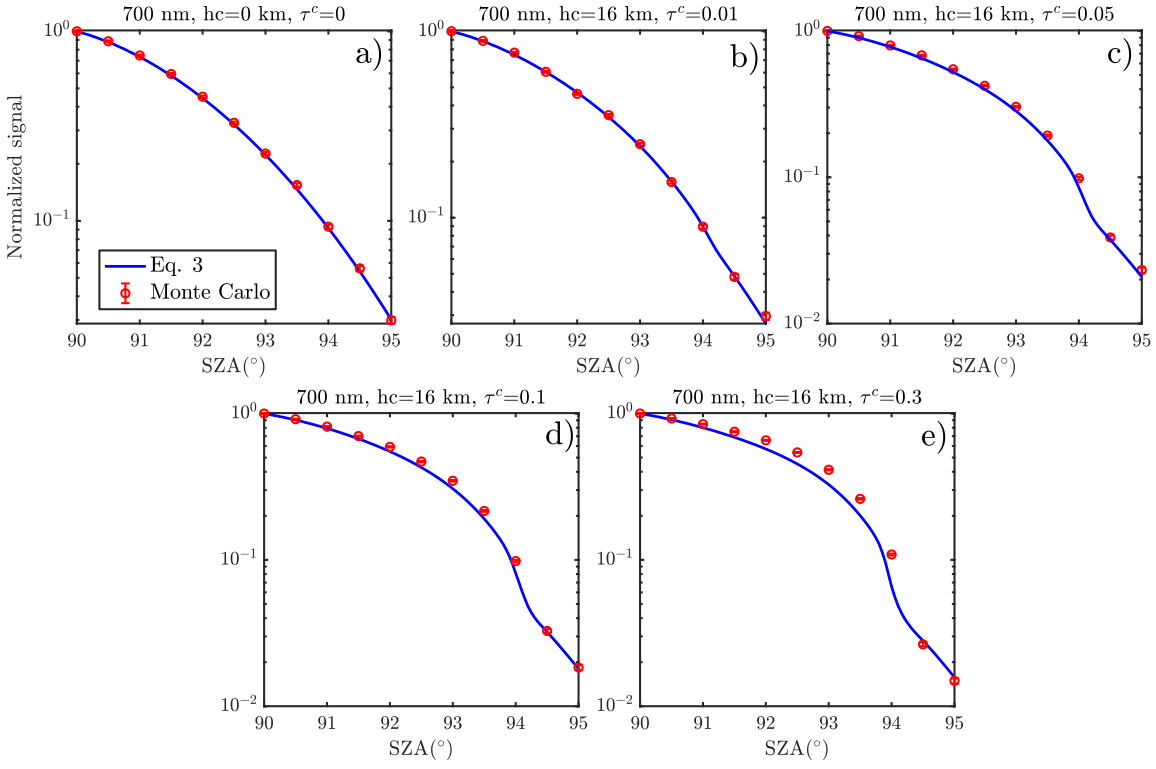

Figure 11. Same as in Fig. 9, but with the cloud height fixed at $h_C = 16$ km and the cloud optical depth varied as follows: $\tau^C = 0$ (panel a), 0.01 (panel b), 0.05 (panel c), 0.1 (panel d), and 0.3 (panel e). All other parameters are identical to those used in Fig. 9.

at longer wavelengths, which would allow the detection of optically thinner clouds. However, since the objective of this section is to intercompare both models rather than to establish a detection limit, the wavelength and cloud optical depth range were fixed accordingly. The comparison shows that the agreement between both models progressively degrades as the cloud optical depth increases. While the SSM reproduces the Monte Carlo results very well for optically thin clouds ($\tau^C \lesssim 0.1$), noticeable differences appear for larger optical depths. These discrepancies can be attributed to multiple-scattering effects within the cloud, which are not accounted for in the SSM.

In order to assess the impact of multiple-scattering effects on the retrieval of cloud height, Fig. 12 shows the relative rate of variation of $P_{\mathrm{Total}}(\lambda, \mathrm{SZA})$ with respect to SZA, computed for $\tau_C = 0.3$ and cloud altitudes of $h_C = 14$, 16, and 18 km. In these simulations, the Monte Carlo calculations were limited to $\mathrm{SZA} < 94°$. This choice is motivated by the high sensitivity of the relative variations of $P_{\mathrm{Total}}(\lambda, \mathrm{SZA})$ to the SZA sampling, which requires a fine angular resolution ($\Delta\mathrm{SZA} = 0.02°$). As a consequence, the computational cost increases significantly as ΔSZA decreases, since a larger number of photons must be simulated to maintain a low level of statistical uncertainty. For this reason, the analysis is restricted to the SZA range of interest around the Rayleigh cutoff, where the determination of $\mathrm{SZA}_{\mathrm{max}}$ is most relevant.

https://doi.org/10.5194/egusphere-2026-2295
Preprint. Discussion started: 26 May 2026

The results show that, despite the differences in the simulated normalized zenith intensities between the Monte Carlo model and the SSM observed in Fig. 11, the relative variations around the Rayleigh cutoff remain very similar in both cases. In particular, differences in $\mathrm{SZA_{max}}$ are found to be on the order of 0.12–0.15°, which, as will be discussed in the following sections, correspond to uncertainties in the retrieved cloud height below 1 km. Thus, we see that for cloud optical depths below $\tau_C \sim 0.3$, the SSM is able to reproduce the Monte Carlo simulations with a satisfactory level of accuracy for the purpose of cloud-height retrieval. For optical depths approaching $\tau_C = 0.3$, the discrepancies increase, leading to uncertainties in cloud height of up to about 1 km. Based on this analysis, we establish that the SSM provides a reliable framework for the interpretation of twilight zenith intensity measurements and the retrieval of cloud heights for $\tau_C \lesssim 0.3$. This range of optical depths is consistent with typical values reported for cirrus and PSCs (see, e.g., Kinne et al., 1989; Gil-Díaz et al., 2024), highlighting the potential of the SSM for application to real observations while avoiding the computational cost of full Monte Carlo simulations.

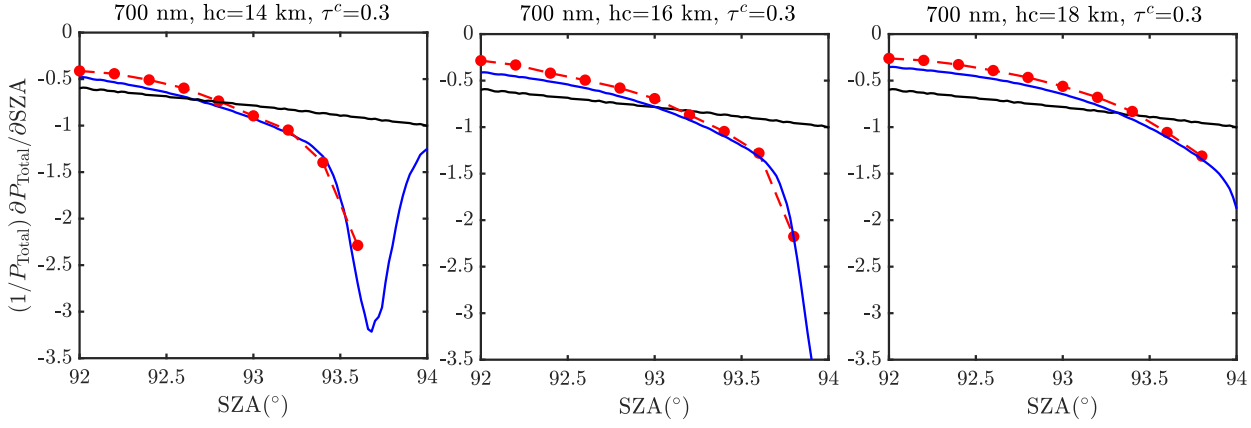

Figure 12. Comparison of the variation of $\left(\frac{1}{P_{\mathrm{Total}}(\lambda,\mathrm{SZA})}\frac{\partial P_{\mathrm{Total}}(\lambda,\mathrm{SZA})}{\partial \mathrm{SZA}}\right)$ with SZA computed using the Monte Carlo model (red dots) and the SSM (blue solid lines) at 700 nm, for a pure Rayleigh atmosphere (black line) and different cloud scenarios with $\tau_C = 0.3$: $h_C = 14$ km (panel a), 16 km (panel b), and 18 km (panel c). All other parameters are identical to those used in Fig. 9.

4 Sensitivity of cloud-height retrieval

Having validated the SSM against Monte Carlo simulations, we now exploit its computational efficiency to investigate how uncertainties in atmospheric and cloud properties propagate into errors in the retrieved cloud height. Such an analysis would be computationally prohibitive using the Monte Carlo model due to its computational cost, but can be systematically explored within the present framework. The goal of this section is therefore to quantify the sensitivity of $\mathrm{SZA_{max}}$, and consequently the inferred cloud height, to assumptions about cloud and atmospheric parameters. We consider a reference atmospheric configuration consisting of a standard Rayleigh atmosphere and a single cloud layer located at 16 km, with an optical thickness of 0.05, a geometrical thickness of 2 km, and a horizontal scale of $R_C = 20$ km. Starting from this baseline scenario, each parameter is

https://doi.org/10.5194/egusphere-2026-2295
Preprint. Discussion started: 26 May 2026

varied individually in order to assess its impact on $\mathrm{SZA_{max}}$. For each perturbation, the resulting shift in $\mathrm{SZA_{max}}$ is computed and subsequently translated into an error in the retrieved cloud height using the model. This approach allows us to directly quantify how uncertainties in atmospheric and cloud properties propagate into biases in cloud height retrieval. Since the CI maximum is determined by the relative SZA-variations of the zenith intensity (Eq. 16), all sensitivity tests are formulated in terms of this quantity rather than the absolute zenith intensity itself. In all simulations, the extinction due to the cloud is included following Eq. 19, thereby accounting for its horizontal distribution.

4.1 Sensitivity to cloud properties

We first investigate the impact of the cloud geometrical thickness on $\mathrm{SZA_{max}}$. Figure 13a shows the relative rate of variation of P_{Total} with respect to SZA at 700 nm for different values of the cloud geometrical thickness, $\Delta h_{\mathrm{C}} = 1, 2, 3$, and 4 km. In each case, $\mathrm{SZA_{max}}$ is defined by the intersection between the corresponding curve and the pure Rayleigh reference (black dashed line). The results show that increasing the cloud geometrical thickness significantly affects both the depth and the width of the minimum. However, these changes occur at SZA values larger than $\mathrm{SZA_{max}}$. At SZAs close to $\mathrm{SZA_{max}}$, all curves nearly overlap, indicating that the position of the CI^R maximum is largely insensitive to variations in Δh_{C}. This behaviour is confirmed quantitatively by the values of $\mathrm{SZA_{max}}$. For a cloud height of 16 km, variations in Δh_{C} lead to changes smaller than 0.05°, which is comparable to the angular resolution used in these simulations. For lower cloud heights (12 and 14 km), slightly larger differences in $\mathrm{SZA_{max}}$ are observed when reducing the geometrical thickness from 2 km to 1 km, reaching up to 0.15° and 0.1°, respectively. However, for $\Delta h_{\mathrm{C}} \geq 2$ km, the variations in $\mathrm{SZA_{max}}$ remain below 0.05° in all cases. These angular differences translate into uncertainties in the cloud height smaller than 1 km.

We next investigate the impact of the cloud horizontal scale, R_{C}. Figure 13b shows an analysis analogous to that in Figure 13a,

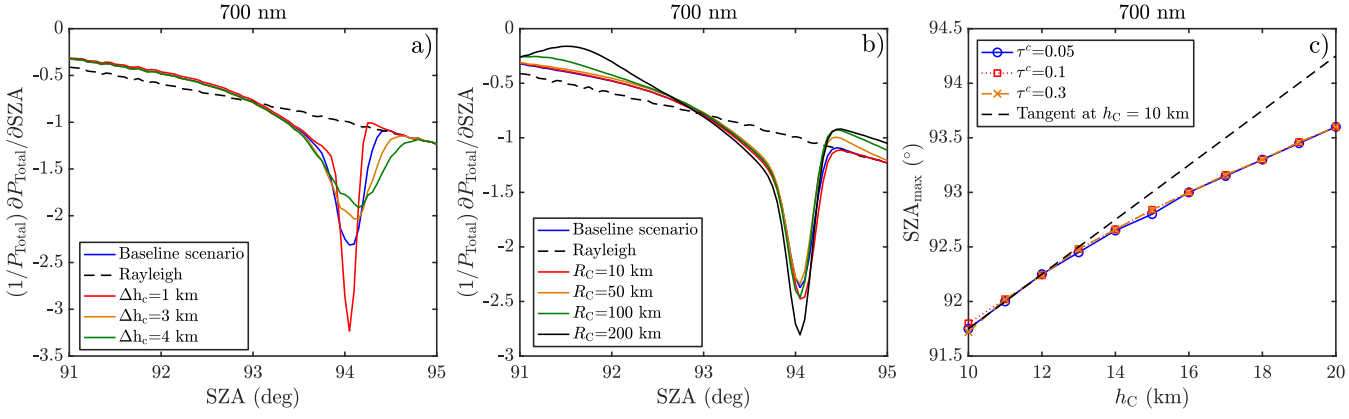

Figure 13. Sensitivity of $\mathrm{SZA_{max}}$ to cloud parameters: (a) variation with cloud geometrical thickness Δh_{C}, (b) variation with cloud horizontal scale R_{C}, and (c) relationship between cloud height and $\mathrm{SZA_{max}}$ for different cloud optical depths. The black dashed line in panel (c) represents the tangent to the $\tau_{\mathrm{C}} = 0.05$ curve at $h_{\mathrm{C}} = 10$ km.

https://doi.org/10.5194/egusphere-2026-2295
Preprint. Discussion started: 26 May 2026

but varying R_C from the baseline value of 20 km to 10, 50, 100, and 200 km. In all cases, the cloud height is fixed at 16 km and the optical thickness at $\tau_C = 0.05$. As expected, R_C has a noticeable impact on the relative SZA-variations of P_{Total}. As R_C increases, the extinction experienced by photons scattered along the line of sight becomes larger, reducing the contribution of P_1. This results in a deeper minimum and modifies the shape of the curves. However, in the SZA range between approximately 92.5° and 93°, all curves tend to converge. Importantly, this convergence occurs close to the intersection with the pure Rayleigh curve, which defines SZA_{max}. As a result, the variations in SZA_{max} remain limited despite the significant changes in the curve shape. By comparing the different cases, we obtain a maximum variation of $\Delta\text{SZA}_{\text{max}} \approx 0.1°$, which translates into an uncertainty in cloud height of approximately 800 m. Similar analyses performed for other cloud heights show that the variations in SZA_{max} can reach up to 0.2° for $h_C = 12$ km. This increase is consistent with the fact that, at lower altitudes, the CI maximum occurs at smaller SZA, where the solar beam propagates more horizontally and traverses a larger portion of the cloud before scattering. Despite these larger angular differences, the resulting uncertainty in cloud height remains of the same order (800 m).

To better understand this behavior, Figure 13c shows the variation of SZA_{max} as a function of cloud height for $\tau_C = 0.05$, $\tau_C = 0.1$, and $\tau_C = 0.3$. The figure also includes the tangent to the $\tau_C = 0.05$ curve at $h_C = 10$ km. It can be seen that the h_C–SZA_{max} relationship systematically lies below this tangent, indicating a sub-linear behavior. This implies that the sensitivity of SZA_{max} to cloud height decreases as altitude increases. This explains why, in the R_C sensitivity test, a variation of $\Delta\text{SZA}_{\text{max}} \approx 0.2°$ at 12 km leads to a cloud-height variation comparable to that produced by a smaller $\Delta\text{SZA}_{\text{max}} \approx 0.1°$ at 16 km. Figure 13c also shows that the h_C–SZA_{max} relationship remains essentially unchanged when the only parameter varied is the cloud optical thickness. This indicates that, in practical applications, τ_C can be kept fixed without introducing significant errors in the cloud-height retrieval. Consequently, any residual uncertainty associated with this parameter is expected to arise primarily from the use of the single-scattering model instead of the Monte Carlo approach. As shown in Section 3.5, these differences remain small and become only noticeable for optically thicker clouds ($\tau_C \sim 0.3$), while still leading to cloud-height uncertainties below 1 km.

Finally, we investigate the impact of the cloud phase function on SZA_{max}. In particular, phase functions are computed using droxtals following the model of Yang et al. (2003, 2013), considering effective radii $r_{\text{eff}} = 5,\ 10$, and 20 μm. In this context, r_{eff} does not correspond to the effective radius of a volume-equivalent sphere, but rather to a geometrical parameter of a lognormal distribution defined in terms of the maximum crystal dimension (D_{max}), with $r = D_{\text{max}}/2$. For the baseline scenario, the resulting values of SZA_{max} are 92.92°, 92.96°, and 93.00° for the three considered values of r_{eff}. According to the h_C–SZA_{max} relationship shown in Figure 13c, these variations correspond to changes in cloud height of less than ∼300 m. These results indicate that the impact of the cloud phase function on the retrieval is non-negligible, but remains smaller than that of other parameters explored in this study. Therefore, uncertainties associated with the microphysical properties of the cloud particles are expected to have a secondary influence on the retrieved cloud height.

4.2 Sensitivity to aerosol properties

In all simulations presented so far, we have considered a pure Rayleigh atmosphere together with the presence of a cloud layer. The next step is to investigate the impact of aerosols on SZA_{max}, and consequently on the retrieved cloud height. To this end,

https://doi.org/10.5194/egusphere-2026-2295
Preprint. Discussion started: 26 May 2026

aerosols are introduced as a vertically distributed layer with an exponential decay characterized by a scale height H^{A}. The aerosol optical depth at the surface, τ_0^{A}, together with H^{A}, are varied in order to assess their influence on the results.

Figure 14 shows the variation of $\mathrm{SZA_{max}}$ with wavelength for a cloud layer with fixed altitude and optical depth of 16 km and

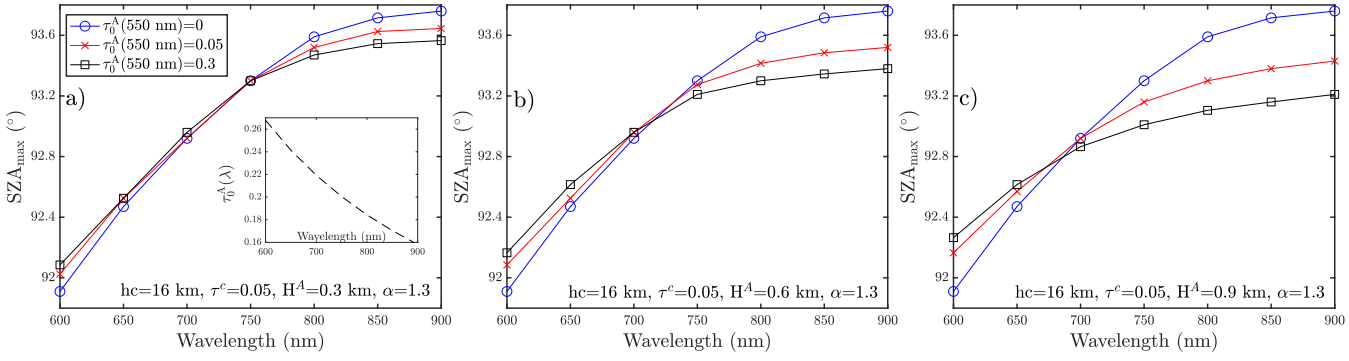

Figure 14. Variation of $\mathrm{SZA_{max}}$ with wavelength derived from CI^R for a cloud layer located at $h_C = 16$ km with optical depth $\tau_C = 0.05$. Results are shown for different aerosol scenarios characterized by $\tau_0^{\mathrm{A}}(550\,\mathrm{nm}) = 0$ (blue line), 0.05 (red line), and 0.3 (black line), and for three aerosol scale heights: $H^{\mathrm{A}} = 0.3$ km (panel a), 0.6 km (panel b), and 0.9 km (panel c). The spectral dependence of τ_0^{A} is parameterized using an Ångström exponent $\alpha = 1.3$, whose corresponding curve is shown in the inset of panel (a).

0.05, respectively. Different values of aerosol optical depth, $\tau_0^{\mathrm{A}}(550\,\mathrm{nm}) = 0,\ 0.05,\ 0.3$, and scale height, $H^{\mathrm{A}} = 0.3$ km, 0.6 km, and 0.9 km, are considered. In these simulations, the spectral dependence of the aerosol optical depth is described using an Ångström exponent of $\alpha = 1.3$. The results show that both the aerosol optical depth and the scale height have a clear impact on $\mathrm{SZA_{max}}$, and therefore on the inferred cloud height. This effect becomes more pronounced at longer wavelengths ($\lambda \gtrsim 750$ nm), where the Rayleigh optical depth is significantly reduced and the relative contribution of aerosols to the total attenuation becomes more important. However, as shown in Figure 14, noticeable differences are also present at shorter wavelengths (e.g. 600 nm), indicating that aerosol effects are not negligible even in the visible range. To investigate the impact of the Ångström exponent on $\mathrm{SZA_{max}}$, Fig. 15 shows simulations similar to those in Fig. 14, but for $\alpha = 0.5$. In this case, the aerosol optical depth decreases more slowly with wavelength over the spectral range considered, resulting in larger values at longer wavelengths. As in the previous case, larger values of τ_0^{A} and H^{A} lead to stronger variations in $\mathrm{SZA_{max}}$, reaching up to $\sim 0.6°$ at $\lambda = 900$ nm for $H^{\mathrm{A}} = 0.9$ km and $\tau_0^{\mathrm{A}}(550\,\mathrm{nm}) = 0$ and 0.3. By contrast, only minor differences are observed when varying the Ångström exponent between $\alpha = 1.3$ and $\alpha = 0.5$ (comparison between Figure 14 and Figure 15), indicating that τ_0^{A} and H^{A} are the dominant parameters controlling the variability of $\mathrm{SZA_{max}}$ in these simulations.

To quantify the impact on the retrieved cloud height, we use a relationship similar to that shown in Fig. 13c. Under this assumption, a variation of $\Delta\mathrm{SZA_{max}} = 0.6°$ corresponds to an uncertainty of approximately 4 km in cloud altitude. This implies that, in a realistic aerosol scenario with $\tau_0^{\mathrm{A}}(550\,\mathrm{nm}) = 0.3$ and $H^{\mathrm{A}} = 0.9$ km, neglecting aerosols in the analysis (i.e., assuming $\tau_0^{\mathrm{A}}(550\,\mathrm{nm}) = 0$) would lead to an error of about 4 km in the retrieved cloud height. However, at 650-700 nm the variations in $\mathrm{SZA_{max}}$ are significantly smaller, with maximum values of $\sim 0.08 - 0.14°$ for $H^{\mathrm{A}} = 0.9$ km and $\tau_0^{\mathrm{A}}(550\,\mathrm{nm}) = 0$ and 0.3.

https://doi.org/10.5194/egusphere-2026-2295
Preprint. Discussion started: 26 May 2026

These variations in $\mathrm{SZA_{max}}$ correspond to uncertainties of approximately 300-700 m in the retrieved cloud height. For smaller values of H^{A}, the differences in $\mathrm{SZA_{max}}$ tend to zero, and therefore the influence of aerosols on the cloud-height retrieval becomes negligible.

These examples demonstrate that, depending on the observational configuration (i.e., number of channels and selected

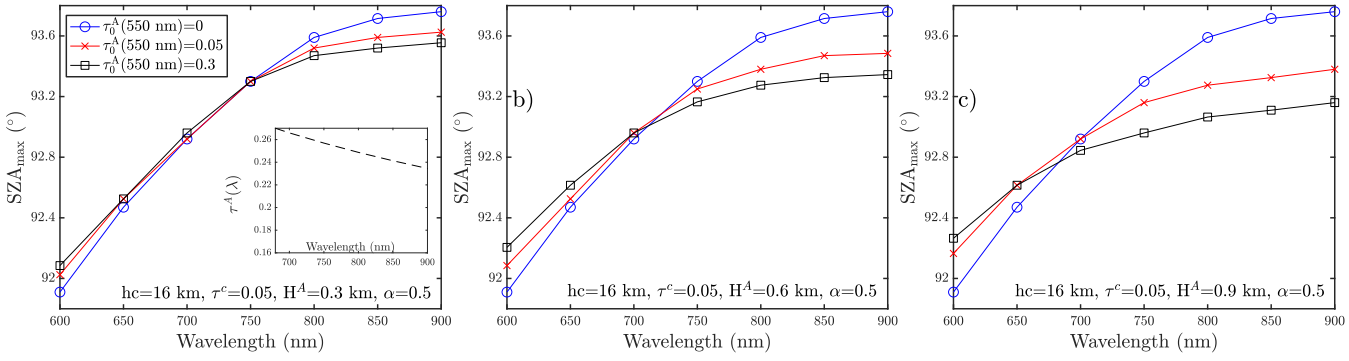

Figure 15. Same as in Fig. 14, but with an Ångström exponent $\alpha = 0.5$.

wavelengths), the presence of aerosols and their vertical distribution can significantly affect the retrieval of cloud height. In this context, the selection of wavelengths around 650-700 nm is preferable, as indicated by the results presented above. However, due to the increase in Rayleigh optical depth at shorter wavelengths, the detection of lower-altitude clouds (below ~ 16 km) becomes progressively more challenging as shorter wavelengths are considered. Multi-wavelength observations in the 650–900 nm spectral range provide an optimal compromise. Such observations would allow the spectral variation of $\mathrm{SZA_{max}}$ to be exploited in order to improve the accuracy of cloud-height retrievals, taking into account not only the presence of aerosols but also other cloud properties analyzed in the previous section.

These results highlight that analyses of this type are essential for defining an optimal cloud-height retrieval strategy tailored to a given observational configuration. In this context, the use of the SSM is particularly advantageous due to its negligible computational cost compared to Monte Carlo RT models. In practice, the computational efficiency of the SSM enables extensive sensitivity studies across a wide range of atmospheric scenarios, including variations in aerosol load, vertical distribution, and wavelength selection. Moreover, given its validity for optically thin clouds ($\tau^{\mathrm{C}} \lesssim 0.3$), the SSM allows full spectral simulations over the visible range to be performed at very low computational cost.

Finally, in the previous section, the differences between the SSM and the Monte Carlo model were shown to become significant mainly for cloud optical depths of $\tau^{\mathrm{C}} \gtrsim 0.3$, due to multiple-scattering effects within the cloud that are not included in the SSM and that primarily affect the scattering term P_2. By contrast, the aerosol contribution enters mainly through P_1, for which the SSM reproduces the pure-Rayleigh behaviour accurately. Therefore, as long as the cloud optical depth remains within the range established in Section 3.5, the agreement between the SSM and the Monte Carlo model is not expected to change substantially

https://doi.org/10.5194/egusphere-2026-2295
Preprint. Discussion started: 26 May 2026

in the presence of aerosols. This further supports the use of the SSM as a reliable and efficient tool for exploring the impact of aerosols and other atmospheric parameters on cloud-height retrievals.

5 Conclusions

In this paper, we have presented a methodology based on the single-scattering approximation for the analysis of the color index (CI), defined in Eq. 1, derived from zenith intensity measurements during twilight for the study of high-altitude clouds. Based on the analysis carried out with this methodology, and its comparison with a Monte Carlo multiple-scattering model in spherical geometry, we derive the following main conclusions:

- The presence of high-altitude clouds during twilight produces a maximum in the CI (for $\lambda_1 < \lambda_2$), whose position in terms of solar zenith angle (SZA) depends on the cloud altitude. The cloud introduces an additional scattering layer that enhances the zenith intensity at both wavelengths. However, due to the wavelength dependence of Rayleigh opacity, the attenuation of the signal is stronger at shorter wavelengths. As a result, the cloud becomes effectively dark at λ_1 at smaller SZAs than at λ_2, leading to an increase of the CI with SZA. This behaviour can be understood from the geometry of the solar path: for a given cloud altitude, the solar rays reaching the cloud traverse progressively lower atmospheric layers as SZA increases, resulting in a larger optical depth along the path. The CI reaches its maximum when the cloud contribution at λ_2 also starts to vanish. The exact value of SZA at CI maximum ($\mathrm{SZA}_{\mathrm{max}}$) corresponds to the condition where the relative variation of the zenith intensity with respect to SZA is equal at both wavelengths. This condition provides a direct physical interpretation of the origin of the CI maximum, linking it to the differential attenuation of radiation at the two wavelengths.

- The detection of clouds using the CI improves as the spectral separation between λ_1 and λ_2 increases. This is due to the strong wavelength dependence of Rayleigh opacity in the visible range: for wavelengths around $\lambda_1 \sim 400$ nm, the Rayleigh optical depth is significant, which reduces the relative contribution of the cloud at λ_1 compared to λ_2. This leads to a stronger enhancement of the CI. In contrast, when both wavelengths are located in the red or near-infrared region (e.g., 700 and 800 nm), the cloud contribution is clearly visible at both wavelengths, resulting in a less pronounced CI maximum. Motivated by this behaviour, we define a new index, the Rayleigh-referenced color index, CI^R. Instead of using measurements at two wavelengths during the same twilight, this index relies on a single wavelength $\lambda = \lambda_2$, while the reference signal at λ_1 is replaced by the corresponding signal at λ_2 for a pure Rayleigh atmosphere. As in the case of the CI, the maximum of CI^R occurs at the SZA for which the relative variations of the zenith intensity with respect to SZA become equal, providing a consistent physical interpretation of the index. This index presents some advantages over the traditional CI:

  (i) Only measurements at a single wavelength are required, allowing the use of narrow-band or single-wavelength instruments. For spectrometers, it also facilitates the selection of spectral regions free from strong gaseous absorption features;

https://doi.org/10.5194/egusphere-2026-2295
Preprint. Discussion started: 26 May 2026

(ii) The contrast of the cloud detection is enhanced in CI^R, since the Rayleigh reference does not include any cloud contribution. This advantage is particularly relevant when the instrument does not allow for a sufficient spectral separation between λ_1 and λ_2, in which case the performance of the traditional CI may be reduced.

- The single-scattering methodology (SSM) was compared with a reference Monte Carlo (MC) radiative transfer model previously used for twilight studies in the atmospheres of the Earth, Mars, and Titan. The comparison shows that the single-scattering approximation provides similar results for cloud optical depths up to $\tau^{\mathrm{C}} \approx 0.3$. For $\tau^{\mathrm{C}} = 0.3$, differences in $\mathrm{SZA}_{\mathrm{max}}$ of about $0.1°$–$0.2°$ are observed, which translate into errors in the retrieved cloud altitude smaller than 1 km. The main advantage of the SSM is its significantly lower computational cost compared to the Monte Carlo model, allowing the efficient exploration of a large number of simulations at different wavelengths and for different cloud geometries. Therefore, for cloud optical depths $\tau^{\mathrm{C}} \leq 0.3$, which is a representative range for high-altitude clouds such as cirrus or polar stratospheric clouds, the SSM provides a powerful and efficient tool for the rapid analysis of twilight zenith observations.

- Sensitivity tests were performed to assess the impact of the main cloud parameters on the retrieval of cloud altitude. In the model, the horizontal distribution of the cloud is assumed to follow a Gaussian profile, analogous to the vertical distribution, with the cloud extinction decreasing with distance from the observer zenith. In addition to the cloud optical depth and altitude, the model includes the parameters Δh_{C} and R_{C}, which define the vertical thickness and horizontal extent of the cloud, respectively. Variations of Δh_{C} between 1 and 4 km, and of R_{C} between 10 and 200 km, result in differences in the retrieved cloud altitude of approximately 800 m. In contrast, no significant variations in $\mathrm{SZA}_{\mathrm{max}}$ are observed when the cloud optical depth is varied between $\tau^{\mathrm{C}} = 0.05$ and 0.3. The impact of the cloud particle phase function was also evaluated by varying the effective radius between 5 and 20 μm. This results in changes in $\mathrm{SZA}_{\mathrm{max}}$ equivalent to variations in the retrieved cloud altitude of about 300 m.

- Sensitivity analyses of aerosol properties show that aerosols can have a significant impact on the retrieval of cloud altitude, even for low optical depths. In particular, the aerosol optical depth τ_0^{A} and scale height H^{A} are identified as the dominant parameters controlling the variability of $\mathrm{SZA}_{\mathrm{max}}$, while the dependence on the Ångström exponent is comparatively weak. In the absence of independent information on aerosol properties, the selection of wavelengths less affected by aerosols, such as those around 650-700 nm, is recommended. Alternatively, the use of representative seasonal aerosol conditions may help reduce potential biases. In any case, the uncertainty in the retrieved cloud altitude associated with aerosol presence should be quantified, particularly in terms of τ_0^{A} and H^{A}, as these parameters can introduce errors of several kilometers under realistic atmospheric conditions.

The conclusions of this work are based on the comparison between the SSM and a Monte Carlo RT model previously validated for similar atmospheric conditions. Future work will focus on the application of this formulation to radiometric measurements, with the aim of directly validating the retrievals against independent cloud-height observations from lidar systems.

https://doi.org/10.5194/egusphere-2026-2295
Preprint. Discussion started: 26 May 2026

Data availability. The scripts used to perform all simulations presented in this study are publicly available at (Toledo, 2026). They enable the full reproducibility of the results shown in the manuscript.

Author contributions. The author conceived the study, developed the methodology, performed the simulations, analyzed the results, and wrote the manuscript.

Competing interests. The author declares that no competing interests are present.

Acknowledgements. This work has been funded by the Spanish Ministry of Science and Innovation through the grant PID2022-139386OA-I00.

https://doi.org/10.5194/egusphere-2026-2295
Preprint. Discussion started: 26 May 2026

References

J. Burrows, A. Dehn, B. Deters, S. Himmelmann, A. Richter, S. Voigt, and J. Orphal. Atmospheric remote-sensing reference data from gome: Part 1. temperature-dependent absorption cross-sections of no2 in the 231–794 nm range. *Journal of Quantitative Spectroscopy and Radiative Transfer*, 60(6):1025–1031, 1998.

C. Gil-Díaz, M. Sicard, A. Comerón, D. C. F. dos Santos Oliveira, C. Muñoz-Porcar, A. Rodríguez-Gómez, J. R. Lewis, E. J. Welton, and S. Lolli. Geometrical and optical properties of cirrus clouds in barcelona, spain: analysis with the two-way transmittance method of 4 years of lidar measurements. *Atmospheric Measurement Techniques*, 17(4):1197–1216, 2024.

L. Gomez-Martin, D. Toledo, C. Prados-Roman, J. A. Adame, H. Ochoa, and M. Yela. Polar stratospheric clouds detection at belgrano ii antarctic station with visible ground-based spectroscopic measurements. *Remote Sensing*, 13(8):1412, 2021.

D. L. Hartmann, J. R. Holton, and Q. Fu. The heat balance of the tropical tropopause, cirrus, and stratospheric dehydration. *Geophysical Research Letters*, 28(10):1969–1972, 2001. https://doi.org/https://doi.org/10.1029/2000GL012833. URL https://agupubs.onlinelibrary.wiley.com/doi/abs/10.1029/2000GL012833.

S. Kinne, O. Toon, G. Toon, C. Farmer, E. Browell, and M. McCormick. Measurements of size and composition of particles in polar stratospheric clouds from infrared solar absorption spectra. *Journal of Geophysical Research: Atmospheres*, 94(D14):16481–16491, 1989.

B. Lauster, S. Dörner, C.-F. Enell, U. Frieß, M. Gu, J. Puķīte, U. Raffalski, and T. Wagner. Occurrence of polar stratospheric clouds as derived from ground-based zenith doas observations using the colour index. *Atmospheric Chemistry and Physics*, 22(24):15925–15942, 2022.

L. Molina and M. Molina. Absolute absorption cross sections of ozone in the 185-to 350-nm wavelength range. *Journal of Geophysical Research: Atmospheres*, 91(D13):14501–14508, 1986.

V. Ramanathan, R. Cess, E. Harrison, P. Minnis, B. Barkstrom, E. Ahmad, and D. Hartmann. Cloud-radiative forcing and climate: Results from the earth radiation budget experiment. *Science*, 243(4887):57–63, 1989.

A. Sarkissian, J. Pommereau, and F. Goutail. Identification of polar stratospheric clouds from the ground by visible spectrometry. *Geophysical research letters*, 18(4):779–782, 1991.

R. Spang, L. Hoffmann, R. Müller, J.-U. Grooß, I. Tritscher, M. Höpfner, M. Pitts, A. Orr, and M. Riese. A climatology of polar stratospheric cloud composition between 2002 and 2012 based on mipas/envisat observations. *Atmospheric Chemistry and Physics*, 18(7):5089–5113, 2018.

D. Toledo. Code for: On the origin of the twilight color index maximum and its application to cloud-height retrieval, Apr. 2026. URL https://doi.org/10.5281/zenodo.19682745.

D. Toledo, P. Rannou, J. Pommereau, A. Sarkissian, and T. Foujols. Measurement of aerosol optical depth and sub-visual cloud detection using the optical depth sensor(ods). atmos. *Meas. Tech. http://dx. doi. org/10.5194/amt-9-455-2016*, 2016.

D. Toledo, L. Gómez, V. Apéstigue, I. Arruego, M. Smith, A. Munguira, G. Martinez, P. Patel, A. Sanchez-Lavega, M. Lemmon, et al. Twilight mesospheric clouds in jezero as observed by meda radiation and dust sensor (rds). *Journal of Geophysical Research: Planets*, 128(7): e2023JE007785, 2023.

D. Toledo, P. Rannou, V. Apéstigue, R. Rodriguez-Veloso, I. Arruego, G. Martínez, L. Tamppari, A. Munguira, R. Lorenz, A. Stcherbinine, et al. Drying of the martian mesosphere during aphelion induced by lower temperatures. *Communications Earth & Environment*, 5(1):717, 2024.

R. West, A. Del Genio, J. Barbara, D. Toledo, P. Lavvas, P. Rannou, E. Turtle, and J. Perry. Cassini imaging science subsystem observations of titan's south polar cloud. *Icarus*, 270:399–408, 2016.

https://doi.org/10.5194/egusphere-2026-2295
Preprint. Discussion started: 26 May 2026

D. M. Winker, M. A. Vaughan, A. Omar, Y. Hu, K. A. Powell, Z. Liu, W. H. Hunt, and S. A. Young. Overview of the calipso mission and caliop data processing algorithms. *Journal of Atmospheric and Oceanic Technology*, 26(11):2310–2323, 2009.

585 P. Yang, B. A. Baum, A. J. Heymsfield, Y. X. Hu, H.-L. Huang, S.-C. Tsay, and S. Ackerman. Single-scattering properties of droxtals. *Journal of Quantitative Spectroscopy and Radiative Transfer*, 79:1159–1169, 2003.

P. Yang, L. Bi, B. A. Baum, K.-N. Liou, G. W. Kattawar, M. I. Mishchenko, and B. Cole. Spectrally consistent scattering, absorption, and polarization properties of atmospheric ice crystals at wavelengths from 0.2 to 100 μ m. *Journal of the atmospheric sciences*, 70(1):330–347, 2013.